Annex A

The annex starts with a section giving an estimate of the necessary energy to displace the ambient gas atmosphere caused by the expansion of the laser-induced plasma. The following sections list the abbreviations and symbols used in this book. The most relevant Stark data for the spectroscopic determination of the electron density of LIBS plasmas are compiled in Sect. A.4. Lists of wavelengths and elements are provided in Sect. A.5. Finally, Sect. A.6 describes a method to select spectral lines for Boltzmann plots.

A.1 Displacement of Ambient Atmosphere

As shown in Sect. 8.1 and Table 8.2 more than 97% of the ambient atmosphere particles are displaced by the expanding laser-induced plasma. A result which is consistent with the simulations presented in Sect. 10.3, Fig. 10.5. In the following the energy necessary for the displacement of the ambient atmosphere will be estimated.

The irradiated laser beam evaporates target material. The particles flowing off collide with particles of the ambient atmosphere. By these collisions, the ambient atmosphere is partially displaced. A part of the ambient gas particles diffuses into the material vapor (cf. Table 8.2, Fig. 10.5). For simplicity, it is assumed that the ambient atmosphere is displaced completely by the expanding material vapor.

In case of a complete displacement, the material vapor and plasma has to do work, which will be calculated taking the following assumptions (a) spherical expansion, (b) the ambient gas is collected at the front of the expanding plasma. The latter is a simplification and yields an upper estimate for the displacement energy (a more realistic description would have to consider the flow of ambient gas induced by the expanding vapor). Then the expanding plasma has to provide the energy given by:

$$E_{\mathrm{d}} = \int_0^R F \,\mathrm{d}r = \int_0^R \frac{\mathrm{d}}{\mathrm{d}t}\left(m_{\mathrm{a}}\dot{r}\right)\mathrm{d}r \tag{A.1}$$

R. Noll, *Laser-Induced Breakdown Spectroscopy*, DOI 10.1007/978-3-642-20668-9,

© Springer-Verlag Berlin Heidelberg 2012

with E_d displacement energy, R radius of the expanding plasma, m_a accumulated mass of ambient gas, $\dot{r}$ velocity of the accumulated ambient gas at the expanding plasma front.

For the accumulated mass of the ambient gas and a half sphere holds:

$$m_\mathrm{a}(t) = \rho_\mathrm{a} \frac{2\pi}{3} r(t)^3, \tag{A.2}$$

where ρ_a is the density of the ambient gas. Insertion of relation (A.2) into (A.1) leads to:

$$E_\mathrm{d} = \frac{2\pi\rho_a}{3} \int_0^R \left(r^3\ddot{r} + 3r^2\dot{r}^2\right)\mathrm{d}r. \tag{A.3}$$

The second integrand can be transformed as follows:

$$\int 3r^2\dot{r}^2\mathrm{d}r = \int \dot{r}^2\mathrm{d}r^3 = \dot{r}^2r^3 - \int r^3\mathrm{d}\dot{r}^2 = \dot{r}^2r^3 - 2\int r^3\ddot{r}\mathrm{d}r \tag{A.4}$$

which yields for (A.3):

$$E_\mathrm{d} = \frac{2\pi\rho_\mathrm{a}}{3}\left(r^3\dot{r}^2 - \int r^3\ddot{r}\mathrm{d}r\right)\Bigg|_0^R \tag{A.5}$$

The kinetic energy of the accumulated gas at the front of the material vapor is given by:

$$E_\mathrm{kin} = \frac{1}{2}\frac{2\pi\rho_\mathrm{a}}{3} R^3\dot{R}^2. \tag{A.6}$$

Relations (A.5) and (A.6) show that for negligible acceleration of the front of the expanding material vapor, i.e., the second term in (A.5) can be neglected, the displacement work is just twice as much as the kinetic energy of the accumulated gas. This case is equivalent to a completely inelastic collision of the ambient gas at the front of the expanding vapor. In the rest frame of the expanding front, the incoming ambient gas loses its kinetic energy being transformed completely into internal energy.

Since the expanding material vapor has a high temperature, it emits visible radiation. In the following it is assumed that the position of the expanding front is identical to the position of the luminous front observed experimentally, cf. Sect. 8.1.

The height of the luminous front is observed with high-speed streak images in the time interval between 3 and 65 ns after the irradiation of the laser pulse with an energy of 40 mJ, see Fig. 8.6. Figure A.1 shows this data in a linear–linear presentation and a second degree polynomial as fit curve.

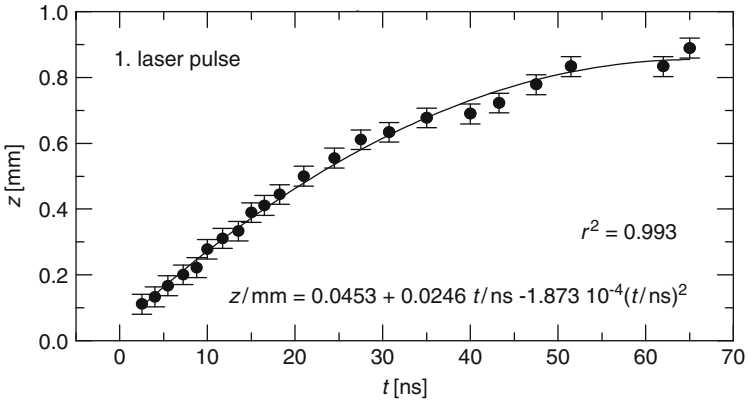

Fig. A.1 Height z of the luminous plasma front above the sample surface as a function of time after the irradiation of the first laser pulse with 40 mJ pulse energy (same data as Fig. 8.6 *top*, but linear scaling of x- and y-axis). As fit curve a second degree polynomial is taken

The general form of the polynomial is given by:

$$r = a_0 + a_1 t + a_2 t^2 \tag{A.7}$$

with (A.5) follows:

$$E_\mathrm{d} = \frac{2\pi\rho_\mathrm{a}}{3}\left(R^3\dot{R}^2 - \frac{a_2}{2}R^4\right) \tag{A.8}$$

with the fit parameters given in Fig. A.1: $a_0 = 0.0453\,\mathrm{mm}$, $a_1 = 0.0246\,\mathrm{mm/ns}$, $a_2 = -1.873\times10^{-4}\,\mathrm{mm/ns^2}$ and the density of air $1.29\,\mathrm{kg/m^3}$ relation (A.8) yields $E_\mathrm{d} = 150\,\mathrm{mJ}$ for $t = 30\,\mathrm{ns}$. This estimate of the upper limit of the displacement energy is higher than the laser pulse energy. Hence, the assumption of a complete displacement and accumulation of the ambient gas at the expanding front is a too strong simplification. Anyway, this estimate shows that the displacement energy is of the same order of magnitude as the laser pulse energy itself. An estimate of the necessary energy to heat the ablated mass of the iron target of about 100 ng (for a single laser pulse with 40 mJ, cf. Fig. 7.5) from room temperature to the melting point (average specific heat capacity of iron 0.8 J/(gK), melt temperature 1,535°C), provision of the melt enthalpy (270 J/g), heating of the melt to the evaporation temperature (assuming the same heat capacity as for solid iron [A.8]), provision of the enthalpy of vaporization (6,370 J/g), heating the vapor to 10,000 K, and ionizing 90% of the Fe particles (ionization energy 7.9 eV) yields 2.1 mJ. Therefore, the displacement energy is significantly greater than the energy necessary to produce the plasma state.

A.2 Abbreviations

Abbreviation	Explanation	Chapter(s)/Section(s)	Page(s)
AAS	Atomic absorption spectroscopy	14.1.2, 14.5	286, 338
ABS	Acrylonitrile butadiene styrene	14.1.2	286
AOM	Acousto-optic modulator	8.1	120
BAS	Bureau of Analysed Samples Ltd.	6.1, 13.1.2	86, 238
BBA	Borate bead analysis	14.2.2	316
BEC	Background equivalent concentration	11.2, 12, 13.1.3	215, 227, 250
BFR	Brominated flame retardants	14.1.2	285
BNC	Bayonet Neill Concelman	13.1.1	231
CARS	Coherent Anti-Stokes Raman spectroscopy	1	1
CCD	Charge-coupled device	4.2, 4.4, 15.1	55, 62, 388
CE	Capillary electrophoresis	2.4, 14.5	14, 338
COG	Curves-of-growths	10, 14.8.2	189, 376
CPC	Condensation particle counter	14.8.2	373
CRM	Certified reference material	2.1	11
DLVQ	Dynamic learning vector quantization	14.1.1	278
DMA	Differential mobility analyzer	14.8.2	373
DP	Double pulses	3.2, 7.3, 11.1	23, 104, 209
DPSSL	Diode-pumped solid state laser	3.1, 3.6, 4.1, 15.1	19, 35, 47, 389
EDL	Electrodeless discharge lamps	12	225
EDXRF	Energy dispersive X-ray fluorescence analysis	14.3	321
ELPI	Electrical low-pressure impactor	14.8.1	362
EOL-WEEE	End-of-life electric and electronic equipment	14.1.2	285
EPMA	Electron probe microscopy	18.3	483
ESMA	Electron scanning microanalysis	18.3	482
fb	Free–bound	8.4	161
ff	Free–free	8.4	161
FHG	Fourth harmonic generation	4.1	48
FML	Flexible measuring system based on LIBS	17.3	448

(continued)

(continued)

Abbreviation	Explanation	Chapter(s)/Section(s)	Page(s)
FWHM	Full width at half maximum	2.1, 3.1, 4.3, 6.2, 9.4, 13.1.1, 14.1.1	10, 19, 59, 92, 173, 230, 281
GC	Gas chromatography	14.5	338
GD-OES	Glow discharge optical emission spectrometry	14.1.2, 16.1, 16.2	286, 401, 416
GF	Graphite furnace	12	224
HDPE	High density polyethylene	14.1.1	278
H_γ	Hydrogen Balmer line	8.2	149
HPLC	High pressure liquid chromatography	2.4, 14.5	14, 338
HPTLC	High performance thin layer chromatography	14.5	338
HWHM	Half width at half maximum	8.2, 14.4	151, 332
ICP-AES	Inductively coupled plasma atomic emission spectrometry	14.1.2	286
ICP-MS	Inductively coupled plasma mass spectrometry	14.1.2, 14.5	286, 347
ICP-OES	Inductively coupled plasma optical emission spectrometry	12, 14.1.2	227, 302
IEC	International Electrotechnical Commission	18.1	468
ILT	Fraunhofer-Institut für Lasertechnik	Preface, 4.5	v, 66
IPDA	Intensified photodiode array	14.1.1	277
IR	Infrared	14.4, 14.5	334, 338
LA-MS	Laser ablation mass spectrometry	14.1.2	286
LAS	Laser absorption spectroscopy	1	3
LDPE	Low density polyethylene	14.1.1	278
LEAFS	Laser-excited atomic fluorescence spectrometry	12, 14.3	221, 320
LIBS	Laser-induced breakdown spectroscopy	1	2
LIDAR	Light detection and ranging	1	1
LIF	Laser-induced fluorescence	1, 12	1, 3, 221
LIFT	Laser identification of fittings and tubes	17.2, 18.1	438, 467

(continued)

(continued)

Abbreviation	Explanation	Chapter(s)/Section(s)	Page(s)
LOD	Limit of detection	11.2, 13.1.1, 13.1.2, 13.3, 14.1.2, 14.3, 17.3, 17.4	215, 234, 240, 267, 299, 323, 451, 462
LOQ	Limit of quantification	11.2	215
LTE	Local temperature equilibrium	8.4, 10	162, 187
MCI	Multichannel integrator electronics	4.5, 13.1.1	66, 231
MCP	Microchannel plate	4.2, 4.4	52, 62, 64
μ−XRF	Micro X-ray fluorescence analysis	18.3	474
MS	Mass spectrometry	14.5	338
MVDA	Multivariate data analysis	16.1	408
NBS	National Bureau of Standards	13.2	254
NCS	National Analysis Center for Iron and Steel	13.2	254
Nd:YAG	Neodymium-doped yttrium aluminum garnet	3.1	17
NIR	Near infrared	14.1.1	276
NIST	National Institute of Standards and Technology	13.1.2	238
NMR	Nuclear magnetic resonance	14.5	338
OES	Optical emission spectrometry	13.1.2	235
PA	Polyamide	3.3	27
PC	Polycarbonate,	3.3	27
	Principal component,	18.3	480
	Personal computer	17.1	435
PCA	Principal component analysis	18.3	478
PDA	Photodiode array	4.2, 15.1	53, 388
PE	Polyethylene	14.1.1	275
PET	Polyethylene terephthalate	14.1.1	275
PIN	Positive-intrinsic-negative photodiode	14.1.1	276
PLS	Partial least squares	16.1, 18.2	409, 471
PMT	Photomultiplier tube	3.5, 4.3, 4.4	30, 53, 61
PP	Polypropylene	14.1.1	275
PS	Polystyrene	14.1.1	275
PVC	Polyvinyl chloride	14.1.1	275

(continued)

(continued)

Abbreviation	Explanation	Chapter(s)/Section(s)	Page(s)
Q-switch	Variable attenuator to influence the quality factor of the laser resonator	4.1, 6	47, 83
RMSE	Root mean square error	16.1	409
RMSEP	Root mean square error of prediction	18.2	471
ROI	Region of interest	14.1.1	280
RR	Rautaruukki Oyj	14.7	358
RSD	Relative standard deviation	3.1, 14.1.2	20, 291
RSDP	Relative standard deviation of procedure	13.3	266
SBS	Stimulated Brillouin scattering	4.3	61
SD-OES	Spark discharge optical emission spectrometry	13.1, 13.1.3, 17.1, 18.3	229, 245, 430, 475
SEM	Scanning electron microscopy	1, 7.1, 15.1	3, 98, 393
SEM-EDX	Scanning electron microscopy energy dispersive X-ray fluorescence analysis	1, 18.3	3, 474
SFC	Supercritical fluid chromatography	14.5	338
SFM	Sum frequency mixing	12	223
SHG	Second harmonic generation	4.1, 12	48, 223
SML	Scanning microanalysis with laser spectrometry	15.2, 18.3	396, 473
SMPS	Scanning mobility particle sizer	14.8.2	373
SNR	Signal-to-noise ratio	14.1.2	288
SP	Single pulses	3.2, 11.1	23, 209
Spark-OES	Spark optical emission spectrometry	17.2	438
TEA	Transverse excited amplifier	14.5	350
TKS	ThyssenKrupp Steel	14.7, 16.1	358, 404
TP	Triple pulses	3.2, 7.3	25, 104
UV	Ultraviolet	3.5	33
VUV	Vacuum ultraviolet	3.5, 13.1.1	32, 230
XRF	X-ray fluorescence analysis	13.1, 13.1.2, 13.1.3, 16.1	229, 235, 245, 401

A.3 List of Symbols

Symbol	Description	Unit	Chapter(s), Section(s), Figure(s), Formula(s)	Page(s)
A	Absorptance	1	5.1, (5.1)	75
A	Dimensionless coefficient for Stark effect	1	9.4, (9.19)	173
A	Analytical resolving power, analytical resolution	1	14.1.2, (14.1), (14.4), 17.2, (17.1), Table 17.5	288, 291, 443
A	ion broadening parameter	1	A.4, Table A.1	512, 514
A_o	Overlapping area	m^2	3.6, Fig 3.20	37
A_C	Effective cross section of measuring chamber	m^2	4.6, Fig 4.17	67
A_{nm}, A_{ji}	Einstein coefficient of the transition $n \rightarrow m$, $j \rightarrow i$	s^{-1}	8.2, (8.5)	133
			9.2, (9.3), (9.8), 10.2, (10.13)	169, 170, 194
A_p	Surface area of a plasma sphere	m^2	9.2, (9.10)	171
A_s	Sampling area	m^2	3.6	38
α, $\alpha^{\nu}(\nu), \alpha^{\lambda}(\lambda)$	Absorption coefficient	m^{-1}	5.3, (5.8)	79
			9.3, (9.11)	171
			9.4, (9.32)	180
α	Angle of incidence	°	4.2, Fig 4.4, (4.1)	51, 52
α	Fine structure constant	1	9.1, (9.1), 10.2, (10.15)	167, 195
a_0	Bohr radius	m	9.1, (9.1), 10.2, (10.15)	167, 195
α_O	Angle of observation	°	3.7, Fig 3.23	39
α_D	Detection angle	°	4.6, Fig 4.18, 13.1.2	68, 237
α_j	Polarizability of species j	m^{-3}	8.3, (8.12)	154
α_L	Angle of incidence of the laser beam	°	3.7, Fig 3.23	39
			3.9, Fig 3.26	42
β	Angle of diffraction	°	4.2, Fig 4.4, (4.1)	51, 52
B_{nm}	Einstein's coefficient of stimulated emission	m/kg	10.2, (10.12)	194
B_{ij}, B_{mn}	Einstein's transition probability for absorption	m/kg	9.3, (9.11)	171
			10.2, (10.12), (10.13)	194, 195
c	Vacuum speed of light	m/s	5.3, (5.8)	79
			9.2, (9.8)	170
c	Specific heat capacity	J/(kg K)	5.1, ((5.2)	75
c_j, c_a	Concentration of analyte j, a	g/g	2.1, 10	11, 192

(continued)

(continued)

Symbol	Description	Unit	Chapter(s), Section(s), Figure(s), Formula(s)	Page(s)
$\hat{c}_i$	Concentration ratio	1	11.5, (11.23), (11.24); 13.2, (13.2)	218, 254
C_s	Stark broadening parameter	$\text{Å}10^{-16}$ cm^3	A.4, Table A.1	512, 514
χ	Adiabatic coefficient	1	8.3, (8.10)	140
d	Diameter of laser beam	m	3.3, (3.5)	28
d	Stark shift	Å	A.4, Table A.1	512, 514
d_s	Single spot diameter	m	3.6	38
d_f	Foil thickness	m	7.4, (7.1)	114
d_g	Grating period	m	4.2, (4.1)	51
d_mc	Diameter of material cloud	m	3.1, (3.1)	21
d_plasma	Diameter of the spherical plasma	m	10, (10.1)	191
$\mathrm{d}A_\mathrm{s}$	Receiving entrance aperture of the spectrometer	m^2	10.2, (10.24)	197
D	Diameter of the illuminated aperture of the focusing lens	m	3.4, (3.3); 11.1, Table 11.1	27, 209
D	Stark shift parameter	m	9.4, (9.20)	174
D_s	Stark shift parameter	$\text{Å}10^{-16}$ cm^3	A.4, Table A.1	512, 514
D_g	Effective diameter of the grating	m	4.2, Fig 4.5, (4.5)	52
$\delta(y,z,t)$	Fringe displacement	1	8.3, (8.11)	154
δ_h	Heat penetration depth	m	3.3, Fig. 3.10, (3.2)	26
			3.6, (3.7)	34
δ_opt	Optical penetration depth	m	3.3, Fig. 3.10	26
			5.1, Fig. 5.1, (5.3)	77
ΔE_z^ion, $\Delta E_{a,z}^\mathrm{ion}$	Lowering of the ionization energy, for species a	J	9.2, (9.7), Fig. 9.2	170
			10.2, (10.5)	193
$\Delta\lambda$	Difference between two neighboring spectral lines of equal intensity	m	4.2, (4.3)	51
$\Delta\lambda^a$	Apparative broadening given as full width at half maximum (FWHM)	m	10.1, Table 10.1, 10.2, (10.24)	192, 197
$\Delta\lambda_\mathrm{D}$	Doppler line width (FWHM)	m	9.4, (9.18), (9.23), (9.26)	173, 174, 175
$\Delta\lambda_\mathrm{G}^\mathrm{m}$	Measured Gaussian part of the line width	m	9.4, (9.27), Fig 9.7	175, 178

(continued)

(continued)

Symbol	Description	Unit	Chapter(s), Section(s), Figure(s), Formula(s)	Page(s)
$\Delta\lambda_{\mathrm{L}}$	Lorentz line width (FWHM)	m	9.4, (9.26)	175
$\Delta\lambda_{\mathrm{L}}^{\mathrm{a}}$	Apparative broadening described by a Lorentz function	m	9.4, (9.28), (9.29)	177, 178
$\Delta\lambda_{\mathrm{L}}^{\mathrm{m}}$	Measured Lorentzian part of the line width	m	9.4, (9.28), Fig 9.6	177
$\Delta\lambda_{\mathrm{N}}$	Natural line width	m	9.4, (9.26)	175
$\Delta\lambda_{\mathrm{shift}}$	Line shift	m	9.4, (9.20)	174
$\Delta\lambda_{\mathrm{Stark}}$	Stark line width (FWHM)	m	9.4, (9.19), (9.22)	173, 174
$\Delta\lambda_{\mathrm{V}}^{\mathrm{a}}$	Total apparative broadening described by a Voigt profile	m	9.4, (9.29)	178
Δs	Distance between the beam waist location and the surface of the target	m	2.1, Fig 2.2	9
			3.4	29
			3.9, Fig 3.26; 11.1, Table 11.1	42, 210
$\Delta\widetilde{\nu}$	Spectral width of the laser radiation	m^{-1}	1, Table 1.1; 4.3, Table 4.7	3, 61
$\Delta\nu_{\mathrm{H}}$	Full frequency width at half maximum	s^{-1}	9.2, (9.5)	169
$\Delta\nu_{\mathrm{V}}$	Frequency shift of the line maximum in relation to an unperturbed line	s^{-1}	9.2, (9.5)	169
Δt	Interpulse separation	s	3.2, Fig 3.9; 11.1, Table 11.1	25, 209
Δt_i	Interpulse separation between pulse i and pulse $i+1$	s	3.2, Fig 3.9	25
$\Delta t_{\mathrm{LIBS-LIF}}$	Time difference between the LIBS-pulse and the LIF-pulse	s	12	224
e	Elementary charge	As	5.3, (5.9)	79
			8.4, (8.15)	161
			9.2, (9.8)	170
E_{b}	Burst energy, $E_{\mathrm{b}} = \sum_j E_j$	J	3.2; 11.1, Table 11.1	25, 209
E_{H}	Ionization energy of hydrogen, Rydberg constant	eV	8.4, (8.17), (8.19); 9.1, (9.1), (9.2); 10.2, (10.16), (10.18)	163, 164, 167, 168, 195

(continued)

(continued)

Symbol	Description	Unit	Chapter(s), Section(s), Figure(s), Formula(s)	Page(s)
E_j	Energy of pulse j in a pulse burst	J	3.2, 11.1, Table 11.1	25, 209
E_L	Energy of the laser pulse	J	3.1, 3.4, (3.6)	20, 28
E_m	Specific melt enthalpy	J/kg	10, Fig 10.1	186
E_m, E_i	Energy of the lower level m, i	eV	9.3, (9.13); 9.4, (9.33); 14.5, Table 14.14	172, 180, 342
E_n, E_j	Energy of the upper level n, j	eV	8.2, Table 8.1; 9.2, (9.3); 13.1.1, Table 13.1; 13.1.2, Table 13.3	133, 169, 231, 238
E_v	Specific enthalpy of vaporization	J/kg	10, Fig 10.1	186
ε_0	Vacuum permittivity, dielectric constant	As/(Vm)	5.3, (5.9), 8.4, (8.15), 9.2, (9.8)	79, 161, 170
$\varepsilon_{a1,2}$	Weighting factor describing the proportion of an element a in the plasma in relation to its proportion in the specimen	1	10, Table 10.1	192
$\varepsilon_{\mathrm{d,th}}$	Damage threshold radiant exposure	$\mathrm{J/m^2}$	4.3, Table 4.5	59
$\varepsilon_\mathrm{fb}(\lambda)$	Emission coefficient of free–bound transitions	$\mathrm{W/(m^3\,sr\,m)}$	10.2, (10.10), (10.16)	194, 195
$\varepsilon_\mathrm{fb}^{\omega,\mathrm{d}\Omega}$	Emission coefficient for free–bound transitions	$\mathrm{W/(m^3\,sr\,rad\,s^{-1})}$	9.1, (9.2)	168
$\varepsilon_\mathrm{ff}(\lambda)$	Emission coefficient of free–free transitions	$\mathrm{W/(m^3\,sr\,m)}$	10.2, (10.10), (10.14)	194, 195
$\varepsilon_\mathrm{ff}^{\lambda}$	Emission coefficient of free–free transitions	$\mathrm{W/(m^3\,m)}$	9.1	167
$\varepsilon_\mathrm{ff}^{\omega,\mathrm{d}\Omega}$	Emission coefficient of free–free transitions	$\mathrm{W/(m^3\,sr\,rad\,s^{-1})}$	9.1, (9.2)	167
$\varepsilon_{ji}^{\nu,\mathrm{d}\Omega}$	Line emission coefficient	$\mathrm{W/(m^3\,sr\,s^{-1})}$	9.2, (9.3)	169
$\varepsilon_\mathrm{l}(\lambda)$	Line emission coefficient	$\mathrm{W/(m^3 sr\,m)}$	10.2, (10.10), (10.14)	194
η	Degree of overlap	1	3.6, (3.8)	37
f	Focal length of a lens	m	3.4, (3.3)	27
f_B	Boltzmann factor	1	8.2, Table 8.2	136
f_{ij}, f_{mn}	Oscillator strength	1	9.2, (9.8); 9.4, (9.33); 13.1.2, Table 13.3; 13.2, Table 13.14	170, 180, 238, 262
$g_{\mathrm{a,z;n}}$	Statistical weight of excited level n of species a in charge state z	1	10.2, (10.8)	193

(continued)

(continued)

Symbol	Description	Unit	Chapter(s), Section(s), Figure(s), Formula(s)	Page(s)
g_m, g_i	Statistical weight of lower level m, i	1	9.2, (9.8), 9.4, (9.33)	170, 180
g_n, g_j	Statistical weight of the upper level n, j	1	8.2, (8.5); 9.2, (9.3), (9.8)	106, 133, 169, 170
$\gamma(\lambda)$	Nonnormalized shape function	1	9.4, (9.30)	178
$\Gamma(\nu)$	Line profile as a function of the frequency	s	9.2, (9.3), (9.4)	169
$\Gamma_{nm}(\lambda)$	Line profile of the transition $n \rightarrow m$	m^{-1}	10.2, (10.12)	194
$\Gamma_L(\nu)$	Lorentz line profile	s	9.2, (9.5)	169
$\Gamma_V(\lambda)$	Voigt profile	m^{-1}	9.4, (9.23)	174
η(order)	Weighting factor between 0 and 1 describing the fraction of diffracted power for a given order of the grating spectrometer	1	10.1, Table 10.1	192
h	Planck constant	Js	8.4, (8.14)	161
h, h_c	Crater depth	m	7.1, Fig 7.1; 13.1.2, Table 13.5; 16.1, Table 16.1	98, 239, 405
$h\nu_{ji}$	Photon energy of the transition from j to i	J	9.2, (9.3)	169
$\hbar\omega$	Photon energy	J	9.1, (9.1)	167
H	Enthalpy of the plasma	J	10.4, (10.25)	203
I	Irradiance at the location of interaction	W/m^2	1, Table 1.1	3
$I(\lambda)$	Spectral radiance	$W/(m^2 sr\, m)$	10.2, (10.9)	193
$I^{acc}_{analyte}(t_{delay}, t_{int})$	Accumulated analyte signal	a.u.	14.1.2, (14.2)	291
$I_{d,th}$	Damage threshold irradiance	W/m^2	4.3, Table 4.5	59
I_f	Average irradiance at the location of the beam waist	W/m^2	3.4, (3.6)	28
$I(\lambda = \lambda_i, t)$	Spectral intensity of the plasma emission at the wavelength λ_i as a function of time	$W/(m^2\, m)$	2.1, Fig 2.4	10
$I_L(R, t)$	Irradiance of the incident laser beam as a function of coordinate R and time t	W/m^2	10, Fig 10.1	186
$I^i_{\lambda_L}$	Irradiance of the incident laser beam	W/m^2	2.1, Fig 2.2	9

(continued)

(continued)

Symbol	Description	Unit	Chapter(s), Section(s), Figure(s), Formula(s)	Page(s)
$I^{\mathrm{r}}_{\lambda_{\mathrm{L}}}$	Reflected laser irradiance	$\mathrm{W/m^2}$	2.1, Fig 2.2	9
$I^{\mathrm{s}}_{\lambda_L}$	Scattered laser irradiance	$\mathrm{W/m^2}$	2.1, Fig 2.2	9
$I_m(\lambda)$	Calculated spectral radiant flux	W/m	10.2, (10.24)	197
$I_3(\lambda)$	Calculated spectral radiant intensity at radius r_3	W/(m sr)	10.2, (10.24)	197
k_{B}	Boltzmann constant	$\mathrm{JK^{-1}}$	5.3, (5.13)	80
			8.4, (8.14)	161
k_s	Segregation ratio	1	18.3, Table 18.3	483
k_t	Quantity proportional to the absorption coefficient	$\mathrm{m^3}$	9.4, (9.33), Table 9.1	180, 181
κ	Thermal diffusivity	$\mathrm{m^2/s}$	3.3, (3.2)	26
			5.1, (5.2)	75
			7.4, (7.1)	114
$\ln \Lambda$	Coulomb logarithm	1	5.3, (5.13), (5.14)	80
L	Distance between the centers of two adjacent laser beam positions	m	3.6, Fig 3.20	37
$L^{\lambda,\,\mathrm{d}\Omega}$	Spectral radiance of a black body, Planck's law	$\mathrm{W/(m^2 sr\,m)}$	9.2, (9.9); 10.2, (10.19), (10.20)	171, 195
$L^{\lambda_{ji},\,\mathrm{d}\Omega}$	Spectral radiance of a black body at the wavelength of the line transition λ_{ji}	$\mathrm{W/(m^2 sr\,m)}$	9.4, (9.31)	179
λ	Wavelength of the laser radiation	m	3.4, (3.3); 11.1, Table 11.1	27, 209
λ_{B}	Thermal de Broglie wavelength of electrons	m	8.4, (8.14)	161
λ_{exc}	Wavelength of the laser used for excitation	m	1, Table 1.1	3
λ_i	Element-specific wavelength	m	2.1, Fig. 2.4	10
λ_{ji}	Wavelength of the transition from j to i	m	9.2, (9.8)	170
$\lambda_{\mathrm{ji\,0}}$	Central wavelength of the transition from j to i	m	9.4, (9.18)	173
λ_{L}	Landau length	m	8.4, (8.15)	161
Λ_{e}	Thermal de Broglie wavelength of the electrons	m	10.2, (10.5)	193

(continued)

(continued)

Symbol	Description	Unit	Chapter(s), Section(s), Figure(s), Formula(s)	Page(s)
m_e	Electron mass	kg	5.3, (5.9)	79
			8.4, (8.14), (8.19)	161, 164
M	Mass of atoms or ions	kg	8.4, (8.19)	164
M^2	Beam propagation ratio	1	3.3, (3.5), 11.1, Table 11.1	28, 209
M_a	Mass of emitting atom species a	kg	9.4, (9.18)	173
n	Diffraction order	1	4.2, (4.1), (4.3), Fig 4.4	51, 52
n	Principal quantum number	1	8.4, (8.17)	163
			9.1, (9.2)	168
n_a	Refractive index of the ambient atmosphere	1	8.3, (8.11)	154
n_e	Electron density	m^{-3}	5.3, (5.9)	79
			8.2, Table 8.2; 9.4, (9.19), (9.20)	136, 173, 174
n_{Fe}	Total iron density (atoms and ions)	m^{-3}	8.2, Table 8.2, (8.6), Table 8.3	136, 139
$n_{Fe\ I}$	Neutral iron (atoms) density	m^{-3}	8.1	175
$n_{Fe\ II}$	Density of singly ionized iron	m^{-3}	8.1	136
n_i	Density of ions	m^{-3}	5.3, (5.13)	80
n_N	Nitrogen density	m^{-3}	8.2, Table 8.2	136
n_p	Refractive index of the plasma	1	8.3, (8.11)	154
n_{ref}	Refractive index	1	4.2, (4.4)	52
N	Number of illuminated grooves of a grating	1	4.2, (4.3)	51
N	Number of samples	1	11.2, (11.10), (11.12), (11.21), (11.22)	213, 216
N_a^z	Density of ion species a with charge z	m^{-3}	9.1, (9.1)	167
			9.2, (9.3)	169
			10.2, (10.5), (10.6)	193
$N_{a\,1,2}$	Particle density of species a originating from the specimen in sphere 1 or shell 2	m^{-3}	10.1, (10.2), Table 10.1	191, 192

(continued)

(continued)

Symbol	Description	Unit	Chapter(s), Section(s), Figure(s), Formula(s)	Page(s)
$N^g_{a\,1,2}$	Particle density of species a originating from the ambient gas in sphere 1 or shell 2	m^{-3}	10.1, (10.3), Table 10.1	191, 192
$N^g_a(r,t)$	Density of ambient gas of species a	m^{-3}	10, Fig 10.1	186
$N^g_{a\,3}$	Particle density of species a (atoms or molecules) of the ambient gas in shell 3	m^{-3}	10.1, (10.4), Table 10.1	191, 192
N_{abl}, $N_{abl,\,3s}$	Number of ablation bursts	1	7.3, 13.1.2	104, 238
N_D	Number of electrons in the Debye sphere	1	8.4, (8.16)	162
			9.4, (9.19)	173
N_e	Electron density	m^{-3}	8.3, (8.12)	154
			9.1, (9.1), (9.2)	167, 168
			10.1, (10.5), (10.7)	193
N_{Fe}	Number of iron particles	1	8.2, Table 8.2	136
$N_{Fe\,I}$	Number of neutral iron particles	1	8.2, Table 8.2	136
$N_{Fe\,I\,n}$	Number of iron atoms in the upper state n	1	8.2, Table 8.2	136
N_j	Densities of neutral atoms and ionic species	m^{-3}	8.3, (8.12)	154
N_{mp}	Number of measuring pulses	1	3.8,11.1, Table 11.1, 13.1.1, 14.2.1	39, 210, 232, 306
N_p	Number of simultaneously generated plasmas	1	3.6	38
N_{pp}	Number of prepulses	1	3.8; 11.1, Table 11.1; 13.1.1, 14.2.1	39, 210, 232, 306
N_{wu}	Number of warming-up pulses	1	3.8; 11.1, Table 11.1	39, 210
NA_{ES}	Numerical aperture of the spectrometer seen from the entrance slit	1	4.2, (4.4)	52

(continued)

(continued)

Symbol	Description	Unit	Chapter(s), Section(s), Figure(s), Formula(s)	Page(s)
ν	Collision frequency of electrons with ions and atoms	s^{-1}	5.3, (5.8), (5.12)	79, 80
ν_0	Frequency of the line maximum for the unperturbed line	s^{-1}	9.2, (9.5)	169
ν_{ei}	Collision frequency of electrons with ions	s^{-1}	5.3, (5.12), (5.13), 8.1	80, 125
ν_{en}	Collision frequency of electrons with atoms	s^{-1}	5.3, (5.12)	80
			8.1	98
ν_{rep}	Repetition rate of the laser source	Hz	3.1, Fig. 3.1; 11.1, Table 11.1	18, 209
ν_{sound}	Velocity of sound of the ambient gas	m/s	3.1, (3.1)	21
ν_{th}	Thermal velocity of the atoms and ions in the plasma	m/s	10.1, (10.1)	191
ω	Angular frequency	rad/s	5.3, (5.8)	79
ω_{p}	Plasma frequency	rad/s	5.3, (5.9)	79
p_{g}, $p_{\mathrm{g}}(r,t)$	Ambient gas pressure	N/m^2	2.1, Fig. 2.2; 10, 11.1, Table 11.1	9, 186, 211
$Q^{i,r}$	Line ratio of analyte line i to reference line r	1	11.1, (11.2); 11.3, (11.22)	208, 216
$\left\langle Q^{i,r}_{m,j}(k)\right\rangle_{N_{\mathrm{wu}},N_{\mathrm{pp}},N_{\mathrm{mp}}}$	Line ratio averaged over N_{mp}measuring pulses after N_{wu}warming-up pulses and N_{pp} prepulses at a single location k	1	11.1, (11.4)	212
$\left\langle\left\langle Q^{i,r}_{m,j}(k)\right\rangle_{N_{\mathrm{wu}},N_{\mathrm{pp}},N_{\mathrm{mp}}}\right\rangle_K$	As previous symbol but averaged over K locations	1	11.1, (11.5)	212
r	Degree of ionization	1	8.2, Table 8.2, Table 8.3	136, 139
r	Correlation coefficient	1	14.5, Fig 14.60	347
r^2	Coefficient of determination	1	11.5; 13.1.1, Table 13.2; 13.1.3, Table 13.8; 13.3, Table 13.16; 14.3, Table 14.12; 17.3, Table 17.7; 17.4, Table 17.8	219, 234, 251, 267, 323, 451, 462

(continued)

(continued)

Symbol	Description	Unit	Chapter(s), Section(s), Figure(s), Formula(s)	Page(s)
r_1	Radius of plasma core	m	10.1, Table 10.1	192
r_2, r_3	Radius of plasma shells	m	10.1, Table 10.1	192
r_c	Radius of the produced laser crater	m	3.6, (3.7)	34
R	Resolving power of spectrometer	1	4.2, (4.3)	51
R	Reflectivity	1	5.1, (5.3)	77
$R(i)$	Mean residual of element i	g/g	11.3, (11.21); 13.2, Tables 13.10, 13.11	216, 257, 259
R_i	Congruence of element i	g/g	13.1.2, (13.1), Table 13.7	239, 245
RMSEP(i)	Root mean square error of prediction	g/g	18.2, (18.1)	471
RSD(c)	Relative standard deviation of concentration c	%	14.2.1, Fig. 14.29, Table 14.11	304, 314
ρ	Mass density	kg/m^{-3}	5.1, (5.2)	75
ρ_0	Density of the homogeneous undisturbed ambient gas	kg/m^{-3}	8.1, (8.1)	125
$s^{\mathrm{acc}}_{\mathrm{analyte}}(t_{\mathrm{delay}}, t_{\mathrm{int}})$	Standard deviation of the accumulated analyte signal	a.u.	14.1.2, (14.3)	291
s_b	Standard deviation of the measuring values of the blank sample	1	11.2, (11.14)	214
s_1	Distance between entrance slit and mirror	m	4.2, Fig 4.5, (4.5)	52
s_{x0}, s_{c0}	Standard deviation of procedure	g/g	11.1, (11.11); 13.3, (13.4)	213, 267
s_y	Residual standard deviation	1	11.1, (11.12)	213
$S(\lambda)$	Spectrum	J/m	2.1	11
t_{delay}	Delay time between the laser pulse and the start of the integration window	s	2.1, Fig. 2.4; 11.1, Table 11.1	10, 210
t_{exc}	Pulse duration of the laser beam	s	1, Table 1.1	3
$t_{f,\alpha}$	t-Value of a one-sided test, f degrees of freedom, α level of significance	1	11.2, (11.14), (11.15), (11.17)	214, 215

(continued)

(continued)

Symbol	Description	Unit	Chapter(s), Section(s), Figure(s), Formula(s)	Page(s)
t_{fq}	Time between the ignition of the flashlamp and the Q-switching	s	3.1, Fig. 3.3	20
t_{int}	Width of the integration window	s	2.1, Fig. 2.2, Fig. 2.4; 11.1, Table 11.1	9, 10, 211
t_{rep}	Repetition time of laser pulses	s	3.1, (3.1)	21
			8.4, Fig. 8.35	161
$T_{1,2}$	Temperature in sphere 1 and shell 2	K	10.1, Table 10.1	192
T_e	Electron temperature	K	5.3, (5.13), (5.14)	80
			8.4, (8.14), (8.15)	161
T_g	Temperature of the ambient gas assumed to be stationary	K	10.1, Table 10.1	192
T_{ge}	Gas exchange time of the measuring chamber	s	4.6, (4.7)	67
τ	Decay time of plasma	s	10.1, (10.1)	191
$\tau_{e,0}$	Time for population of discrete levels according to Boltzmann statistics for neutrals	s	8.4, Fig 8.35, (8.21)	161, 165
τ_{ee}	Electron–electron relaxation time	s	8.4, Fig 8.35, (8.18)	161, 164
$\tau_{e,z-1}$	Time for population of discrete levels according to Boltzmann statistics for stage of ionization z with $z = 1$ for neutrals, $z = 2$ for singly ionized species	s	8.4, (8.21)	165
τ_{ge}	Local gas exchange time	s	3.1, (3.1)	21
			8.4, Fig 8.35	161
τ_k^0	Electron-neutral relaxation time	s	8.4, (8.19)	164
τ_k^1	Electron-ion relaxation time	s	8.4, (8.20)	164
τ_L	Temporal width (FWHM) of the laser pulse	s	3.1, Fig. 3.3; 3.4, (3.6)	20, 28, 22
			7.4, (7.1); 8.4, Fig 8.35; 11.1, Table 11.1	114, 161, 209

(continued)

(continued)

Symbol	Description	Unit	Chapter(s), Section(s), Figure(s), Formula(s)	Page(s)
$\tau_{\mathrm{L}j}$	Temporal width (FWHM) of the laser pulse j in a pulse burst	s	3.2, Fig 3.9; 11.1, Table 11.1	25, 209
τ_{mod}	Time scale of multiple pulses	s	8.4, Fig 8.35	161
τ_{Plasma}	Life time of plasma	s	8.4, Fig 8.35	161
τ_s^{λ}	Optical thickness of a plasma layer	1	9.3, (9.16)	172
θ_0	Beam divergence angle of a Gaussian beam	rad	3.4, (3.4)	28
Θ	Beam divergence angle (full angle) of the laser beam	rad	3.4, (3.5)	28
$u_a^z(T, \Delta E_{a,z}^{\mathrm{ion}})$	Partition function of species a with charge z as a function of temperature and reduction of ionization energy	1	9.2, (9.3), (9.6); 10.2, (10.5); 11.1, (11.3)	169, 193, 211
$u_{\mathrm{Fe0}}, u_{\mathrm{Fe1}}, u_{\mathrm{N0}}, u_{\mathrm{N1}}$	Partition function of neutral, singly ionized iron; neutral, singly ionized nitrogen	1	10.4, (10.25)	203
u^{S}	Partition function of the plasma state generated with SP	1	8.2, (8.7)	136
u^{D}	Partition function of the plasma state generated with DP	1	8.2, (8.7)	136
U_{osc}	Charging voltage of the capacitors driving the flashlamp	V	3.1, Fig 3.3	20
U_{pc1}	Bias voltage at Pockels cell	V	3.1, Fig 3.3	20
U_{PMT}	Signal of a PMT	V	3.5, Fig 3.13	30
V_{C}	Volume of measuring chamber	m^3	4.6, (4.7)	67
$\dot{V}_{\mathrm{in}}$	Inlet gas flow rate	m^3/s	4.6, Fig 4.17, (4.7)	67
$\dot{V}_{\mathrm{mc}}$	Gas flow rate in the measuring chamber	m^3/s	11.1, Table 11.1	211
V_{p}	Plasma volume	m^3	8.3, (8.11)	154
			9.2, (9.10)	171
V_{x0}	Relative standard deviation of procedure	%	11.1, (11.13)	213
w_0	Radius of beam waist	m	3.4, (3.3)	27

(continued)

(continued)

Symbol	Description	Unit	Chapter(s), Section(s), Figure(s), Formula(s)	Page(s)
w_b	Radius of the beam waist on the surface of the specimen	m	3.6, (3.7), (3.8)	34, 37
w_m	measured full Stark width of the line at the given wavelength	Å	A.4, Table A.1	512, 514
w_{th}	theoretically calculated full Stark width of the line at the given wavelength	Å	A.4, Table A.1	512, 514
W_e	Electron energy	eV	8.4, (8.18)	164
W_{FWHM}	Stark broadening parameter for the full width (FWHM)	m	9.4, (9.19)	173
x	Concentration of reference sample	g/g	11.2, (11.6)	212
x_{ID}	Limit of identification	g/g	11.2, (11.17)	215
x_{LOD}	Limit of detection	g/g	11.2, (11.15), (11.16), (11.17)	215
x_{LOQ}	Limit of quantification	g/g	11.2, (11.18)	215
$\hat{y}$	Prediction of measurand by regression curve	1	11.2, (11.6), (11.7), (11.8)	212
$\overline{\hat{y}'}$	Sensitivity as first derivative of the regression curve at the middle of the working range	g/g	11.2, (11.9)	213
$\bar{y}_b$	Arithmetic average of n measurements of the blank sample	1	11.2, (11.14)	214
y_c	Critical value	1	11.2, (11.14)	214
ξ	Parameter describing the geometry of the energy release and the shock wave expansion	1	8.1, (8.1)	125
z	Ionization stage	1	8.4, (8.17)	163
			9.1, (9.1)	167
z_R	Rayleigh length	m	3.4, Fig 3.12	29
			3.6	33
Z	Ion charge	1	5.3, (5.13)	80
ζ	Skewness	1	18.3, (18.2)	481
$\xi(\lambda)$	Spectral characteristics of the observation channel	1	10.1, Table 10.1, (10.24)	192, 197

A.4 Stark Data

Table A.1 lists a selection of Stark data for various atom and ion emission lines which are useful for diagnostic purposes of laser-induced plasmas (cf. Sect. 9.4). If several values are stated in a reference, then the average value is taken. In [A.4], Stark parameters are calculated for an electron density of 10^{16} cm^3. The calculated widths were multiplied by 2 to obtain the full widths, such as the experimental values given in, e.g., [A.1,A.3]. The experimental values taken from [A.2] and [A.9] were also multiplied by 2 to get the full width. References [A.10–A.20] give further information on Stark data as well as Table 10.2 in Sect. 10.2.

A.5 Wavelengths and Elements

The following compilation of wavelengths and elements provides an overview of those lines investigated for LIBS and described in this book. They were used, e.g., to determine calibration curves, analysis functions, detection limits, standard deviations of procedure, background equivalent concentrations, coefficients of determination, plasma temperatures, electron densities, self-absorption, temporal behavior of analyte emission. Table A.2 is arranged in ascending order of wavelengths starting with vacuum ultraviolet lines and ending in the near infrared with a ratio of the longest to the shortest wavelength of 6.4, i.e., more than two octaves. Table A.3 lists the studied elements in alphabetic order and allocates the observed emission wavelengths. In this way, both tables allow for an easy access to identify lines, their features, and usage. These tables are not intended as a comprehensive overview of emission lines studied so far for LIBS. The reader is referred to the respective literature given in the previous chapters and data bases as, e.g., [13.30, A.21]. With the help of Table A.2, these wavelengths are linked to the respective matrices investigated.

A.6 Spectral Line Selection for Boltzmann Plots

An important method to determine the temperature of laser-induced plasmas is based on the Boltzmann plot, see, e.g., Sect. 8.2, Fig 8.15 and Sect. 13.2, Fig 13.22. The choice of appropriate spectral lines is often based on experience and reference values and can even be restricted by spectroscopic or other hardware equipments. The development of spectrometers with large wavelength ranges, e.g., echelle spectrometers as described in Sect. 4.2, enables the simultaneous detection and acquisition of spectral lines with resolutions better than 20 pm, see Table 4.4 [A.22, A.23]. In the following a basic, quantitative, and objective method for the selection of spectral lines needed for temperature determinations by Boltzmann plots is

Table A.1 List of Stark data

El	IS	λ(nm)	C_s(Å 10^{-16}cm^3)	w_m, w_{th} (Å)	D_s(Å10^{-16} cm^3)	d(Å)	T(K)	n_e (10^{17} cm^{-3})	A	Ref.
Al	II	199.053	0.0440	0.044		n.i.	10,500	0.1	n.i.	[A.2]
Al	II	263.155	0.0640	0.064		n.i.	10,500	0.1	n.i.	[A.2]
Al	II	266.917	0.0062	0.0062		n.i.	10,500	0.1	n.i.	[A.2]
Al	II	281.618	0.0424	0.0424		n.i.	10,500	0.1	n.i.	[A.2]
Al	II	390.068	0.0100	0.01		n.i.	10,500	0.1	n.i.	[A.2]
Al	I	308.215	0.0398	0.51	0.0148	0.19	13,200	1.28	n.i.	[A.1]
Al	I	309.271	0.0398	0.51	0.0469	0.6	13,200	1.28	n.i.	[A.1]
Al	I	394.401	0.0336	0.840	0.0168	0.42	11,700	2.50	n.i.	[A.3]
Al	I	396.152	0.0336	0.840	0.0168	0.42	11,700	2.50	n.i.	[A.3]
Al	II	466.305	0.1206	0.121	0.0651	0.07	10,500	0.10	n.i.	[A.2]
Al	II	559.323	0.3800	0.380		n.i.	10,500	0.10		[A.2]
Al	II	704.206	0.1930	1.930	−0.0690	−0.69	18,000	1.00		[A.3]
Al	II	705.656	0.1870	1.870	−0.0710	−0.71	18,000	1.00		[A.3]
Al	II	706.362	0.1900	1.900	−0.0680	−0.68	18,000	1.00		[A.3]
Ar	II	295.539	0.0900	0.900		n.i.	28,500	1.00	n.i.	[A.3]
Ar	I	415.859	0.1952	1.210		n.i.	11,900	0.62	n.i.	[A.3]
Ar	I	425.936	0.2323	1.440		n.i.	11,900	0.62	n.i.	[A.3]
Ar	I	425,900[a]	0.2600	0.260	0.1320	0.13	10,000	0.10	0.069	[A.4]
Ar	I	427.217	0.1903	1.180		n.i.	11,900	0.62	n.i.	[A.3]
Ar	II	434.81	0.0197	0.197				1.00		[A.3]
Ar	II	457.935	0.0304	0.210	0.0087	0.06	12,000	0.69	n.i.	[A.3]
Ar	I	470.232	0.2136	1.410		n.i.	12,000	0.66	n.i.	[A.3]
Ar	II	514.531	0.5449	3.760	0.1957	1.35	12,000	0.69	n.i.	[A.3]
Ar	I	750.386	1.16					0.1		[A.5]
Ar	I	751.465	1.01					0.1		[A.5]
C	I	165.7[a]	0.0017	0.0165		n.i.	12,500	1.00	n.i.	[A.1]

C	I	165.7[a]	0.0035	0.00348	0.0021	0.0021	10,000	0.10	0.031	[A.4]
C	I	165.812	0.0036	0.060	0.0020	0.0325	14,000	1.65	n.i.	[A.1]
C	I	193.027	0.0044	0.0044	0.0027	0.0027	10,000	0.10	0.03	[A.1]
C	I	193.091	0.0050	0.0300	0.0028	0.017	11,700	0.60	n.i.	[A.1]
			0.0051	0.1120	0.0026	0.057	15,500	2.20	n.i.	[A.1]
Cl	I	725.662	0.1378	0.510		n.i.	10,000	0.37	n.i.	[A.3]
				n.i.	0.0642	0.17	9,500	0.27	n.i.	[A.3]
Cl	I	754.707	0.1486	0.550		n.i.	10,000	0.37	n.i.	[A.3]
				n.i.	0.0642	0.17	9,500	0.27	n.i.	[A.3]
Cu	I	510.554	0.0430	0.430	0.0067	0.07	10,000	1.00	n.i.	[A.3]
Fe	I	373.487	0.0090	0.090			8,000	1.00		[A.6]
Fe	I	376.554	0.0090	0.090			8,000	1.00		[A.6]
Fe	I	376.719	0.0090	0.090			8,000	1.00		[A.6]
Fe	I	378.788	0.0090	0.090			8,000	1.00		[A.6]
Fe	I	381.584	0.0140	0.140			8,000	1.00		[A.6]
Fe	I	492.050	0.1070	0.107		n.i.	8,000	0.10	n.i.	[A.1]
Fe	I	536.7	0.06–0.14				7,400–9,500			[A.7]
Fe	I	538.337	0.2120	0.212		n.i.	9,500	0.10	n.i.	[A.8]
Fe	I	538.3	0.08–0.2				6,600–10,000			[A.7]
Fe	I	540.4	0.07–0.12				7,400–9,500			[A.7]
Fe	I	542.407	0.1300	0.130		n.i.	8,000	0.10	n.i.	[A.1]
Hg	I	435.834	0.0280	0.03		n.i.	6,000	0.1	n.i.	[A.3]
K	I	766.490	0.1240	1.24	0.0275	0.28	20,000	1.0	n.i.	[A.1]

(*continued*)

Table A.1 (continued)

El	IS	λ(nm)	C_s(Å 10^{-16}cm^3)	w_m, w_{th} (Å)	D_s(Å 10^{-16} cm^3)	d(Å)	T(K)	n_e (10^{17} cm^{-3})	A	Ref.
Mg	I	291.545	0.0500	0.50		n.i.	10,000	1.0	n.i.	[A.1]
N	I	149.263	0.0003	0.00034		n.i.	12,350	0.1	n.i.	[A.1]
			0.0003	0.00303	0.0002	0.0016	13,000	1.0	n.i.	[A.1]
N	I	149.3[a]	0.0025	0.0025	0.0015	0.0015	10,000	0.1	0.029	[A.4]
N	I	790.45	2.4000	2.4	0.9000	0.9	10,000	0.1		[A.9]
O	I	130.4[a]	0.0016	0.00164	0.0010	0.001	10,000	0.1	0.028	[A.4]
O	I	777.3[a]	0.0630	0.0630	0.0143	0.0143	10,000	0.1	0.012	[A.4]
P	I	178.0[a]	0.0097	0.0097	0.0053	0.0053	10,000	0.1	0.043	[A.4]
Pb	I	405.781	0.0620	0.620		n.i.	11,600	1.0	n.i.	[A.1]
Si	I	288.2[a]	0.0128	0.0128	0.0079	0.0079	10,000	0.1	0.033	[A.4]

[a] Average wavelength of a multiplet

El = element, IS = ionization stage, C_s = Stark broadening parameter, w_m = measured full width of the line at the given electron density, w_{th} = theoretically calculated full width of the line at the given electron density, D_s = Stark shift parameter (calculated with d/n_e), d = Stark shift, positive if the wavelength is increased, T = temperature of the plasma, A = ion broadening parameter (cf. Sect. 9.4, (9.19), (9.20)), n.i. = no information available

Table A.2 Wavelengths and elements studied for LIBS in this book, allocation to chapters, sections, figures and tables

Wavelength (nm)	Element	Matrix	Chapter(s), Section(s), Figure(s), Table(s)	Page(s)
130.22	O I	Inclusions/steel	18.3, Fig. 18.14	477
134.72	Cl I	Cement	14.4, Fig. 14.44, Fig. 14.46, Fig. 14.49, Fig. 14.50, Fig. 14.51, Fig. 14.52	331, 332, 334, 335, 336
149.26	N I	Inclusions/steel	18.3, Fig. 18.15, Fig. 18.16	478, 479
165.81	C I	Steel	17.1, Table 17.3	438
178.28	P I	Steel, segregation/steel	3.5, Fig. 3.15; 13.1.1, Fig. 13.4, Table 13.2; 13.1.2, Table 13.6; 13.1.3, Fig. 13.15, Table 13.8; 18.3, Fig. 18.22	32, 233, 234, 240, 251, 483
180.73	S I	Steel, segregation/steel	3.5, Fig. 3.15; 13.1.1, Fig. 13.5, Table 13.2; 13.1.2, Table 13.6; 13.1.3, Table 13.8; 15.1, Fig. 15.9; 18.3, Fig. 18.22	32, 234, 240, 251, 397, 483
187.75	Fe II	Steel	3.5, Fig. 3.15; 3.8, Fig. 3.24; 13.1.1, Fig. 13.3, Fig. 13.4, Fig. 13.5; 13.1.2, Fig. 13.8, Fig. 13.9; 13.1.3, Fig. 13.14, Fig. 13.15, Fig. 13.16	32, 40, 233, 234, 241, 242, 250, 251
193.09	C I	Steel, inclusions/steel	3.8, Fig. 3.24; 13.1.1, Fig. 13.2, Fig. 13.3, Table 13.2; 13.1.2, Table 13.6, Fig. 13.8, Fig. 13.9; 13.1.3, Fig. 13.14, Table 13.8; 15.1, Fig. 15.8; 17.1, Table 17.3	40, 232, 233, 234, 240, 241, 242, 250, 251, 396, 438
194.23	Hg II	Mercury lamp	17.4, Fig. 17.29	457
212.41	Si I	Steel	6.1, Fig. 6.5; 15.1, Fig. 15.8, Fig. 15.10	91, 396, 398
213.86	Zn I	Aerosol	14.8.1, Fig. 14.84, Fig. 14.88	369, 371
225.39	Ni II	Steel, high-alloy steel	13.1.2, Table 13.6; 13.2, Table 13.10, Fig. 13.19	240, 257, 258

(continued)

Table A.2 (continued)

Wavelength (nm)	Element	Matrix	Chapter(s), Section(s), Figure(s), Table(s)	Page(s)
228.80	Cd I	Soil, polymer	12, Fig. 12.5, Fig. 12.6; 14.1.2, Table 14.6, Fig. 14.16, Fig. 14.18, Table 14.7, Table 14.8; 14.3, Table 14.12	226, 227, 295, 297, 298, 299, 303, 323
231.60	Ni II	Steel, soil	13.1.1, Table 13.2; 13.1.3, Fig. 13.16, Table 13.8; 14.3, Table 14.12	234, 251, 323
234.98	As I	Soil	14.3, Table 14.12	323
247.86	C I	Polymer, air, grease/aluminum, particulate/top gas	14.1.1, Fig. 14.2; 14.6, Fig. 14.63, Fig. 14.64, Fig. 14.65, Fig. 14.66, Fig. 14.67; 14.8.1, Fig. 14.83; 17.4, Fig. 17.37	279, 352, 353, 354, 368, 463
251.43	Si I	Slag	14.2.2, Fig. 14.33, Fig. 14.34, Fig. 14.37; 18.2, Fig. 18.9	317, 319, 473
251.61	Si I	High-alloy steel	13.2, Fig. 13.20	258
253.65	Hg I	Polymer, soil	14.1.2, Table 14.6, Table 14.7, Table 14.8; 14.3, Table 14.12	295, 299, 303, 323
257.51	Al I	Aluminum, grease/aluminum	14.8.1, Fig. 14.82, Fig. 14.83	367, 368
259.80	Sb I	Polymer	14.1.2, Table 14.6, Table 14.7, Table 14.8	295, 299, 303
259.94	Fe II	Aluminum	13.3, Table 13.15, Table 13.16, Table 13.17, Fig. 13.25	266, 267, 269, 271
263.82	Mn II	Inclusions/steel	15.2, Fig. 15.9; 18.3, Fig. 18.12	397, 476
267.72	Cr II	High-alloy steel steel, aluminum	11.5, Fig. 11.6; 13.1.1, Table 13.2; 13.2, Table 13.10, Table 13.13; 13.3, Table 13.15, Table 13.16, Table 13.17, Table 13.18; 17.2, Table 17.5, Table 17.6	219, 234, 257, 261, 266, 267, 269, 270, 443, 444
271.44	Fe II	High-alloy steel steel, particulate/top gas	11.5, Fig. 11.5; 13.1.1, Table 13.1; 13.2, Fig. 13.19, Fig. 13.20; 14.7, Fig. 14.75	218, 231, 258, 360

(continued)

Table A.2 (continued)

Wavelength (nm)	Element	Matrix	Chapter(s), Section(s), Figure(s), Table(s)	Page(s)
273.07	Fe II	Steel	3.5, Fig. 3.13; 6.1, Fig. 6.3, Fig. 6.5, Fig. 6.6; 17.1, Fig. 17.12; 17.2, Table 17.6	30, 88, 91, 92, 439, 444
273.36	Fe I	High-alloy steel	13.2, Table 13.14	262
278.81	Fe I	High-alloy steel	13.2, Table 13.14	262
279.08	Mg II	Aluminum	9.4, Fig. 9.10; 13.3, Table 13.15, Table 13.16, Table 13.17	181, 266, 267, 269
279.55	Mg II	Aluminum, water	9.4, Fig. 9.10; 14.5, Fig. 14.62; 17.3, Table 17.7	181, 349, 451
281.62	Mo II	Steel, high-alloy steel	13.1.2, Table 13.6; Fig. 13.8; 13.2, Table 13.10; 17.2, Table 17.6	240, 241, 257, 444
286.26	Cr II	High-alloy steel	11.5, Fig. 11.5; 13.2, Table 13.10, Table 13.11	218, 257, 259
288.16	Si I	Aluminum steel	11.2, Fig. 11.2; 13.1.1, Table 13.2; 13.3, Table 13.15, Table 13.16, Table 13.17, Fig. 13.24, Table 13.18; 17.3, Fig. 17.22, Table 17.7	214, 234, 266, 267, 269, 270, 450, 451
289.36	Hg I	Mercury lamp	17.4, Fig. 17.28	457
293.31	Mn II	Steel, pure iron, aluminum	6.1, Fig. 6.4, Fig. 6.6; 13.1.1, Table 13.2; 13.1.2, Table 13.6; 13.3, Table 13.15, Table 13.16, Table 13.17, Table 13.18; 15.1, Fig. 15.10; 17.1, Fig. 17.12	89, 92, 234, 240, 266, 267, 269, 270, 398, 439
294.92	Mn II	Aluminum	17.3, Table 17.7	451
296.12	Cu I	Aluminum	13.3, Table 13.15, Table 13.17, Table 13.18	266, 269, 270
296.69	Fe I	High-alloy steel	13.2, Table 13.14	262
298.92	Cr II	High-alloy steel	17.2, Table 17.6	444

(continued)

Table A.2 (continued)

Wavelength (nm)	Element	Matrix	Chapter(s), Section(s), Figure(s), Table(s)	Page(s)
305.71	Al I	Aluminum	11.2, Fig. 11.2; 13.3, Table 13.15, Fig. 13.24, Fig. 13.25	214, 266, 270, 271
307.21	Zn I	Zinc-coated steel	17.3, Fig. 17.25	454
308.22	Al I	Inclusions/steel	18.3, Fig. 18.13, Fig. 18.15, Fig. 18.16, Fig. 18.17, Fig. 18.18, Fig. 18.21	477, 478, 479, 480, 481
309.27	Al I	Slag	14.2.2, Fig. 14.37; 17.3, Fig. 17.22	319, 450
324.75	Cu I	Copper, steel, high-alloy steel, soil, water, aerosol, aluminum, segregation/steel	7.3, Fig. 7.7; 13.1.2, Table 13.3, Table 13.6; 13.2, Fig. 13.18, Table 13.10; 14.3, Fig. 14.38, Table 14.12; 14.5, Fig. 14.61; 14.8.1, Fig. 14.87; 17.3, Fig. 17.21, Fig. 17.22, Table 17.7; 18.3, Fig. 18.22	105, 238, 240, 256, 257, 322, 323, 348, 371, 450, 451, 483
327.40	Cu I	Aluminum	3.9, Fig. 3.25; 13.3, Table 13.15, Table 13.16, Table 13.17; 17.3, Fig. 17.21	42, 266, 267, 269, 450
328.23	Zn I	Zinc-coated steel	16.1, Table 16.2, Table 16.3, Fig. 16.9	410, 411, 414
334.50	Zn I	Aluminum, soil, particulate/top gas	13.3, Table 13.15; 14.3, Fig. 14.38, Table 14.12; 14.7, Fig. 14.72, Fig. 14.74; 17.3, Table 17.7	266, 322, 323, 358, 360, 451
334.94	Ti II	Aluminum	17.3, Table 17.7	451
337.28	Ti II	Aluminum	13.3, Table 13.15, Table 13.16, Table 13.17, Table 13.18	266, 267, 269, 270
341.48	Ni I	Aluminum	13.3, Table 13.15, Table 13.16, Table 13.17	266, 267, 269
351.92	Tl I	Soil	14.3, Table 14.12, Fig. 14.40, Fig. 14.41	325, 326
356.54	Fe I	High-alloy steel	13.2, Table 13.14, Fig. 13.22	262, 263
357.58	Zr I	Aluminum	17.3, Table 17.7	451
358	CN	Ammonium nitrate	17.4, Fig. 17.37	463
363.15	Fe I	High-alloy steel	13.2, Table 13.14, Fig. 13.22	262, 263

(continued)

Table A.2 (continued)

Wavelength (nm)	Element	Matrix	Chapter(s), Section(s), Figure(s), Table(s)	Page(s)
364.44	Ca I	Slag	14.2.2, Fig. 14.36	319
364.78	Fe I	High-alloy steel	13.2, Table 13.14, Fig. 13.22	262, 263
368.35	Pb I	Aerosol	14.8.1, Fig. 14.85, Fig. 14.86	369, 370
371.99	Fe I	High-alloy steel, aluminum, steel	13.2, Table 13.14, Fig. 13.22; 13.3, Table 13.15, Table 13.17; 15.1, Fig. 15.6, Fig. 15.10; 17.2, Fig. 17.16, Fig. 17.17	262, 263, 266, 269, 394, 398, 445, 446
373.83	Fe I	Aluminum	17.3, Table 17.7, Fig. 17.25	451, 454,
374.95	Fe I	High-alloy steel	13.2, Table 13.14, Fig. 13.22	262, 263
381.30	Fe I	Steel	9.4, Fig. 9.6, Fig. 9.7	177, 178
381.58	Fe I	Steel, aerosol	9.4, Fig. 9.6, Fig. 9.7; 14.8.1, Fig. 14.85, Fig. 14.86	177, 178, 369, 370
382.78	Fe I	Steel	9.4, Fig. 9.6, Fig. 9.7	177, 178
383.83	Mg I	Aluminum	17.3, Table 17.7	451
384.99	Fe I	Steel	9.4, Fig. 9.6, Fig. 9.7	177
387.1	CN	Ammonium nitrate	17.4, Fig. 17.37	463
390.55	Si I	Soil, aluminum, slag	12, Fig. 12.5; 13.3, Table 13.15, Table 13.17; 14.2.1, Fig. 14.27, Fig. 14.28; 14.2.2, Fig. 14.35	226, 266, 269, 309, 310, 318
393.37	Ca II	Water, aerosol, particulate/top gas	14.5, Fig. 14.60; 14.7, 14.8.2, Fig. 14.89, Fig. 14.91, Fig. 14.93, Fig. 14.94	347, 355, 373, 376, 378, 379
394.40	Al I	Aluminum	9.4, Fig. 9.6, Fig. 9.11; 10.2, Fig. 10.6; 17.4, Fig. 17.31	177, 182, 202, 458
396.15	Al I	Steel, zinc-coated steel, ZnAl binary alloy, aluminum, inlcusions/steel	13.1.2, Table 13.6; 16.1, Fig. 16.10; 16.2, Fig. 16.13, Fig. 16.14, Fig. 16.15, Fig. 16.16, Fig. 16.17; 17.4, Fig. 17.31; 18.3, Fig. 18.13, Fig. 18.21	240, 415, 420, 422, 423, 424, 425, 458, 477, 481
396.85	Ca II	Aerosol	14.8.2, Fig. 14.95	380
404.58	Fe I	High-alloy steel	13.2, Table 13.14, Fig. 13.22	262, 263

(continued)

Table A.2 (continued)

Wavelength (nm)	Element	Matrix	Chapter(s), Section(s), Figure(s), Table(s)	Page(s)
405.78	Pb I	Polymer, soil, particulate/top gas	14.1.2, Fig. 14.9, Fig. 14.10, Fig. 14.11, Fig. 14.12, Fig. 14.13, Table 14.6, Fig. 14.14, Fig. 14.15, Table 14.7, Fig. 14.21, Fig. 14.22, Table 14.8; 14.3, Table 14.12; 14.7, Fig. 14.72	290, 293, 294, 295, 299, 301, 303, 323, 358
406.36	Fe I	High-alloy steel	13.2, Table 13.14, Fig. 13.22	262, 263
407.17	Fe I	High-alloy steel	13.2, Table 13.14, Fig. 13.22	262, 263
410.98	Fe I	Zinc-coated steel	16.1, Table 16.3, Fig. 16.9	411, 414
411.85	Fe I	High-alloy steel	13.2, Table 13.14, Fig. 13.22	262, 263
413.47	Fe I	High-alloy steel	13.2, Table 13.14, Fig. 13.22	262, 263
419.91	Fe I	High-alloy steel	13.2, Table 13.14, Fig. 13.22	262, 263
421.94	Fe I	High-alloy steel	13.2, Table 13.14, Fig. 13.22	262, 263
422.67	Ca I	Aerosol	14.8.1, Fig. 14.84	369
425.43	Cr I	Polymer, soil	14.1.2, Table 14.6, Table 14.7, Table 14.8; 14.3, Table 14.12	295, 299, 303, 323
427.18	Fe I	Pure iron, high-alloy steel	8.2, Fig. 8.24; 13.2, Table 13.14, Fig. 13.22	150, 262, 263
430.01	Ar I	Gas	8.2, Fig. 8.24	150
430.79	Fe I	Pure iron, high-alloy steel	8.2, Fig. 8.24; 13.2, Table 13.14, Fig. 13.22	150, 262, 263
432.58	Fe I	Pure iron, high-alloy steel	8.2, Fig. 8.24, Fig. 8.26; 13.2, Table 13.14, Fig. 13.22	150, 152, 262, 263
433.12	Ar II	Gas	8.2, Fig. 8.24	150
434.52	Ar I	Gas	8.2, Fig. 8.24	150
434.81	Ar II	Gas	8.2, Fig. 8.24, Fig. 8.25; 15.1, Fig. 15.7	150, 151, 395
438.35	Fe I	Steel, high-alloy steel, zinc-coated steel	9.4, Fig. 9.5; 13.2, Table 13.14, Fig. 13.22; 16.1, Fig. 16.5, Fig. 16.6, Fig. 16.7, Table 16.2, Table 16.3, Fig. 16.8, Fig. 16.9; 16.2, Fig. 16.16, Fig. 16.17	176, 262, 263, 406, 407, 408, 410, 411, 413, 414, 424, 425

(continued)

Table A.2 (continued)

Wavelength (nm)	Element	Matrix	Chapter(s), Section(s), Figure(s), Table(s)	Page(s)
460.96	Ar II	Gas	15.1, Fig. 15.7	395
472.22	Zn I	Zinc-coated steel, ZnAl binary alloy	16.1, Fig. 16.5, Fig. 16.6, Fig. 16.7, Table. 16.2, Table. 16.3, Fig. 16.8, Fig. 16.9, Fig. 16.10; 16.2, Fig. 16.13, Fig. 16.14, Fig. 16.15, Fig. 16.16, Fig. 16.17	406, 407, 408, 410, 411, 413, 414, 415, 420, 422, 423, 424, 425
473.59	Ar II	Gas	15.1, Fig. 15.7	395
476.49	Ar II	Gas	15.1, Fig. 15.7	395
486.13	H I	Polymer	14.1.1, Fig. 14.2	279
522.72	Fe I	High-alloy steel	13.2, Table 13.14, Fig. 13.22	262, 263
531.66	Fe II	Steel	10.2, Fig. 10.5	198
532.42	Fe I	Steel	8.2, Fig. 8.13, Fig. 8.16, Table 8.3; Fig. 8.19, Fig. 8.20, Fig. 8.21; 10.2, Fig. 10.5	134, 138, 139, 142, 143, 144, 198
532.80	Fe I	Steel	6.3, Fig. 6.7; 8.2, Fig. 8.13, Fig. 8.16; 10.2, Fig. 10.5	93, 134, 138, 198
533.99	Fe I	Steel	10.2, Fig. 10.5	198
534.6	Continuum	Steel	8.2, Fig. 8.22	145
536.29	Fe II	Steel	10.2, Fig. 10.5	198
537.15	Fe I	Steel	8.2, Fig. 8.13, Fig. 8.14; 10.2, Fig. 10.5	134, 198
538.34	Fe I	Steel	8.2, Fig. 8.13, Fig. 8.14, Fig. 8.22; 8.3, Fig. 8.33; 9.1, Fig. 9.1; 9.4, Fig. 9.4, Fig. 9.5, Fig. 9.8, Fig. 9.9; 10.2, Fig. 10.5	134, 145, 158, 168, 176, 179, 180, 198
539.71	Fe I	Steel	8.2, Fig. 8.13; 10.2, Fig. 10.5	134, 198
540.58	Fe I	Steel	8.2, Fig. 8.13	134
589.00	Na I	Water, particulate/top gas, aerosol	14.5, Fig. 14.59; 14.7, Fig. 14.74; 14.8.2, Fig. 14.91, Fig. 14.92, Fig. 14.93	346, 360, 376, 377, 378
589.59	Na I	Water	14.5, Fig. 14.59	346
656.28	H I	Propane/carbon dioxide, particulate/top gas, ammonium nitrate	14.6, Fig. 14.67, Fig. 14.68; 14.7, Fig. 14.73; 17.4, Fig. 17.37	354, 355, 359, 463
725.66	Cl I	Polymer	14.1.1, Fig. 14.6	283

(continued)

Table A.2 (continued)

Wavelength (nm)	Element	Matrix	Chapter(s), Section(s), Figure(s), Table(s)	Page(s)
742.36	N I	Air, ammonium nitrate	14.6, Fig. 14.63; 17.4, Fig. 17.37	352, 463
744.23	N I	Air	14.6, Fig. 14.63	352
746.83	N I	Air, particulate/top gas, inclusions	14.6, Fig. 14.63	352
754.71	Cl I	Polymer	14.1.1, Fig. 14.6	283
766.49	K I	particulate/top gas	14.7	355
777.19	O I	Air/carbon dioxide, particulate/top gas, propane/carbon dioxide, ammonium nitrate, inclusions/steel	14.6, 14.7, Fig. 14.63, Fig. 14.65, Fig. 14.66, Fig. 14.68; 17.4, Fig. 17.37; 18.3, Fig. 18.14, Fig. 18.15, Fig. 18.17, Fig. 18.18	352, 353, 354, 355, 463, 477, 478, 479,480
777.42	O I	Air/carbon dioxide, propane/carbon dioxide	14.6, Fig. 14.63, Fig. 14.65, Fig. 14.66, Fig. 14.68	352, 353, 354, 355
777.54	O I	Air/carbon dioxide, propane carbon dioxide	14.6, Fig. 14.63, Fig. 14.65, Fig. 14.66, Fig. 14.68	352, 353, 354, 355
827.24	Br I	Polymer	14.1.2, Table 14.6, Fig. 14.17, Fig. 14.19, Table 14.7	295, 298, 299
837.59	Cl I	Cement	14.4, Fig. 14.45, Fig. 14.48, Fig. 14.50	331, 334, 335

described [A.24]. This approach implicates advantages especially in those cases where no spectral line experiences or empirical values are available for a specific diagnostic task. Additionally, even for comparatively low laser pulse energies, larger sets of spectral lines can be determined by a systematic approach, which effect a decrease in the relative error of the electron temperature to be determined. Thus, the temporal characterization of the LIBS plasma can be improved and well grounded. Low laser pulse energies are, e.g., used for microanalysis as, e.g., those described in [A.25–A.27] and Chaps. 15, 16.

The experiments are carried out with a flashlamp pumped Q-switched Nd:YAG laser at the fundamental wavelength $\lambda = 1{,}064\,\text{nm}$ and a repetition rate of $\nu_{\text{rep}} = 20\,\text{Hz}$. The laser beam diameter amounts to 6 mm. The pulse duration is about $\tau_{\text{L}} = 5\,\text{ns}$. The pulse energy is attenuated by a Glan-laser-prism and four different laser pulse energies, e.g., 0.2, 0.5, 1, and 2 mJ, are studied. This pulse energy regime is of interest for the design of compact LIBS instrumentation, where the use of more powerful laser sources is not possible or for LIBS in combination with laser micromachining or LIBS microanalysis [A.28,A.29]. All experiments are carried out in air at atmospheric pressure. The samples are certified C75 steel alloy

Table A.3 Elements in alphabetic order and emission wavelengths

Element	Wavelength(s) (nm)
Aluminum	257.51, 305.71, 308.22, 309.27, 394.40, 396.15
Antimony	259.80
Argon	430.01, 433.12, 434.52, 434.81, 460.96, 473.59, 476.49
Arsenic	234.98
Bromine	827.24
Cadmium	228.80
Calcium	364.44, 393.37, 396.85
Carbon	165.81, 193.09, 247.86
Chlorine	134.72, 725.66, 754.71, 837.59
Chromium	267.72, 286.26, 298.92
Copper	296.12, 324.75, 327.40
Hydrogen	486.13, 656.28
Iron	187.75, 259.94, 271.44, 273.07, 273.36, 278.81, 296.69, 356.54, 363.15, 364.78, 371.99, 373.83, 374.95, 381.30, 381.58, 382.78, 384.99, 404.58, 406.36, 407.17, 410.98, 411.85, 413.47, 419.91, 421.94, 422.67, 425.43, 427.18, 430.79, 432.58, 438.35, 522.72, 531.66, 532.42, 532.80, 533.99, 536.29, 537.15, 538.34, 539.71, 540.58
Lead	368.35, 405.78
Magnesium	279.08, 279.55, 383.83
Manganese	263.82, 293.31, 294.92
Mercury	194.23, 253.65, 289.36
Molybdenum	281.62
Nickel	225.39, 231.60, 341.48
Nitrogen	149.26, 742.36, 744.23, 746.83
Oxygen	130.22, 777.19, 777.42, 777.54
Phosphor	178.28
Silicon	212.41, 251.43, 251.61, 288.16, 390.55
Sodium	589.00, 589.59
Sulfur	180.73
Thallium	351.92
Titanium	334.94, 337.28
Zinc	213.86, 307.21, 328.23, 334.50, 472.22
Zirconium	357.58

samples (German designation 1.1750) with low concentrations of C (0.78 m.-%), Cr (0.17 m.-%), Si, (0.28 m.-%), Mn (0.7 m.-%), P (0.009 m.-%), and S (0.005 m.-%). The sample surface was put in a vertical plane and the laser beam was focused horizontally at right angle onto the sample surface by a planoconvex achromatic lens ($f = 50$ mm). The beam waist diameter is about $2w_0 = 23\,\mu$m and the average irradiance at the sample surface amounts to $I_f = 10^{10}, 2.5 \times 10^{10}, 5 \times 10^{10}$, and 10^{11} W/cm^2 for the different pulse energies. The sample is moved by linear axes perpendicularly to the laser beam axis with a speed of 2 mm/min. The plasma is imaged with a reduction ratio of 1 : 0.7 using a concave mirror into an optical fiber with a core diameter of 800 μm connected to the spectrometer. The spectrometer is an echelle system with a spectral resolution of 1–22 pm in the wavelength range

between 200 and 780 nm, cf. Sect. 4.2, Table 4.4. The detection system consisting of spectrometer and optical fiber uses an internal response correction function to achieve a wavelength independent response within its wavelength range. Due to the small emission intensities at laser pulse energies of only a few millijoule 100 consecutive LIBS spectra are accumulated in this wavelength range. To study the time evolution of the plasma, the line emission is investigated at nine different delay times $t_{\mathrm{delay}} = 100 - 900$ ns with an integration time of $t_{\mathrm{int}} = 100$ ns each. The upper limit for the delay time has to be chosen because of the fast decreasing spectral line intensity of the Fe II species. In the case of $E_{\mathrm{b}} = 200\,\mu$J, the $1/e$-decay time of the intensity is about 260 ns. For times up to $t_{\mathrm{delay}} = 900$ ns, a sufficient spectral line intensity can be assured for all studied pulse energies. Thus, for every pulse energy nine spectra corresponding to the nine different time windows were recorded so that in total 36 spectra were obtained for the four laser pulse energies.

Due to the comparatively low laser pulse energies used low emission line intensities are expected. In order to assure a minimum error of the determined electron temperatures, a procedure to find appropriate emission lines for the Boltzmann plots is developed. In a first step of this procedure, a preselection of spectral lines based on theoretical calculations is carried out. Afterwards, these preselected lines are assessed within an iterative optimization step using experimental data in which improper spectral lines are discarded successively. The total number of all atomic and ionic emission lines of elements contained in the used samples within the spectral range of 200–780 nm amounts to ∼93,000 [A.30]. Assuming local thermal equilibrium (LTE) – see Sect. 8.4 – the electron temperature derived by the Boltzmann plot method is independent of the considered species within the plasma. The emission coefficient is proportional to the number density of the particular species in the plasma, cf. Sect. 9.2, (9.3). Thus, in the following only the emission lines of the matrix element, which in this case is Fe (>98 m.-%), are considered to determine the electron temperature using Boltzmann plots. The total number of Fe emission lines amounts to $\sim 38,000$ in the considered spectral range. Electron temperatures in LIBS plasmas are typically in the range of 5,000–16,000 K. The excitation probability decreases with the excitation energy according to the Boltzmann distribution, cf. (9.3). As on average higher ionization stages have higher excitation energies and lower occurrences in the plasma due to the Saha equation [cf. Sect. 10.1, (10.5)], and emissions of Fe lines with ionization stages higher than I and II are negligible for the expected temperature ranges. Hence, the further considered spectral lines are limited to the first two ionization stages Fe I and Fe II. The total number of remaining lines for these two species is about ∼30,000. To reduce this huge number of spectral lines to only those which are clearly identifiable in the whole spectrum, it is reasonable to develop a criterion based on the emission coefficients of the spectral lines. For the remaining Fe I and Fe II spectral lines, the emission coefficients can be calculated according to the relationship (9.3). The partition function for each species can be obtained for example from the Atomic Spectral Database of the National Institute of Standards and Technology [A.21]. The electron temperature T_{e} can be estimated or derived from preliminary measurements. Here, the following temperatures were chosen:

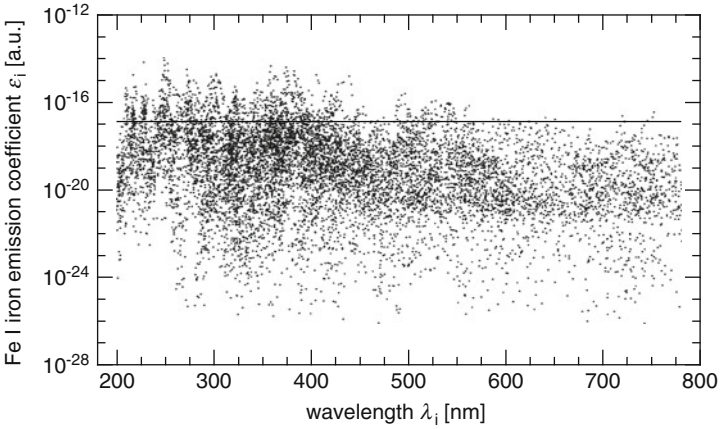

Fig. A.2 Calculated emission coefficients for all Fe I spectral lines in the considered wavelength range. The *horizontal line* represents the threshold value (mean value of all emission coefficients) for this species. The index i characterizes the individual Fe I emission line

$T_e = 8{,}900\,\mathrm{K}$ for Fe I emission lines and $T_e = 11{,}300\,\mathrm{K}$ for Fe II emission lines, respectively. In order to extract the lines with the highest emission coefficients, threshold values are calculated for each species, Fe I and Fe II. As particular threshold value the mean value of all emission lines of the regarded species is taken. The number density N can be set to a constant value, since only emission lines of the same species are compared with each other. Figure A.2 shows the half-logarithmic plot of calculated emission coefficients for Fe I emission lines versus their wavelength.

After discarding all emission lines with lower emission coefficients than the chosen threshold value in total 966 Fe I and 585 Fe II emission lines can be identified as potential candidates for the Boltzmann plots. In a second step, these remaining spectral lines have to be assessed quantitatively with respect to superposition and overlapping with other spectral lines.

Spectral lines emitted by the laser-induced plasma are broadened by a variety of mechanisms such as Stark, Van-der-Waals and Doppler broadening, cf. Sect. 9.4. Additionally, the apparative broadening of the spectrometer increases the widths of all spectral lines as well, see, e.g., Figs. 9.6 and 9.7.

Since the Boltzmann plot method relies on the measured emission line intensity, it is necessary to identify those lines which do not significantly overlap with other emission lines, e.g., due to line broadening mechanisms. Therefore, in the next step each of the remaining Fe I and Fe II lines is investigated with respect to superpositions with other emission lines which can occur in the plasma. This investigation has to cover all present species and elements in the sample even if the concentration is comparatively low. In our case for each of the remaining Fe I and Fe II emission lines a wavelength interval of 200 pm is centered at the transition wavelength λ_k. The emission coefficients ε_i of all other spectral lines within this

wavelength interval are summed up according to

$$U_k = \sum_i \varepsilon_i . \tag{A.9}$$

for all i with $|\lambda_i - \lambda_k| \leq 100\,\text{pm}$ and $i \neq k$.

Afterwards, this sum of all emission coefficients in the 100 pm-neighborhood of the considered Fe emission line is compared with the emission coefficient at λ_k. Only those emission lines which fulfill the condition

$$\varepsilon_k > 3 \cdot U_k \tag{A.10}$$

are retained. With this condition, it is assured that each remaining emission line does not interfere significantly with other spectral lines within the chosen neighborhood. Even if there are still interfering emission lines, the condition (A.10) ensures that the disturbing lines have a cumulative emission coefficient of less than a third of the emission coefficient ε_k at λ_k. By this preselection for the above-described case 337 Fe I and 96 Fe II spectral lines are obtained as potential candidates for the electron temperature determination. It might happen that some of these remaining lines have the same upper energy level. In this case, only those spectral lines are retained with the highest ε_k / U_k ratio. All other lines of the same energy level are discarded, since otherwise particular energy levels would be preferred in the Boltzmann plot. By eliminating spectral lines with the same upper energy level 199 Fe I and 64 Fe II emission lines are obtained as an intermediate result after the successive preselection processes. The average ε_k / U_k ratios amount to 191.3 for Fe I and 239.7 for Fe II. As mentioned above, this result shows that even if overlapped lines are not discarded by the proposed method and used criteria, the contribution of the disturbing lines to the emission coefficient would theoretically be less than 1% and can therefore be neglected. Finally, comparing all initially regarded iron lines (9,922 Fe I, 20,162 Fe II) only 0.87% are further considered after the preselection.

After the preselection procedure, the line intensities of these emission lines have to be determined from experimentally recorded spectra in order to generate Boltzmann plots. The line profile is divided in three wavelength intervals marked with A, B, and C. Interval B contains the peak of the line and ranges in-between the closest local minima on either side of the peak. Adjacent on both sides of interval B are the intervals A and C with an extent of 10 pm each. To account for background noise of the detection system the average intensity in the intervals A and C is subtracted from the line intensity in interval B. The background corrected net line intensity can then be determined via trapezoidal integration. However, some of the preselected lines might not be detectable, visible or identifiable due to various reasons. In the case described here, the echelle spectrometer has gaps in its detectable wavelength range. Additionally, some lines may disappear in the continuum radiation emitted by the plasma which was not considered in the theoretical part as well. After eliminating emission lines which were predicted as

prominent in the spectrum but not present in one of the 36 experimentally recorded spectra 167 Fe I and 48 Fe II emission lines were clearly identified and allocated.

With the spectral line intensities determined, the electron temperatures were deduced via Boltzmann plots for every time window and laser pulse energy. The relative error of the electron temperature averaged over the 36 spectra amounts to $\Delta T_e/T_e = 4.9\%$ ($r^2 = 0.72$) for Fe I lines and $\Delta T_e/T_e = 61.2\%$ ($r^2 = 0.06$) for Fe II lines. The coefficients of determination are rather poor, for iron ion lines the situation is worse compared with iron atomic lines. Some data points are far away from the regression curve. To eliminate outliers in the Boltzmann plot, an iterative method to discard spectral lines which do not match with the overall trend given by the other data points was developed. The goal of this method is to identify a set of lines for the specific time domain and pulse energy regime based on an algorithm which considers the residuum of an individual data point in the Boltzmann plot from the regression line, i.e., its distance in y-direction. For each spectral line, the following measure is calculated to ensure that the used spectral line has an emission intensity level high enough to allow detection within the entire specified time domain and pulse energy regime:

$$S_k = \sum_{x,y} D_{k,x,y}^2. \tag{A.11}$$

The indices x and y are for the different time windows and pulse energies. The index k denotes the individual spectral lines and $D_{k,x,y}$ are the deviations between a data point and the regression line. S_k corresponds to the total sum of the squared deviations for all time windows and laser pulse energies. Thus, the spectral line with the maximum value for S_k has on average, e.g., in the considered case for all four laser pulse energies and for all nine time windows, the largest deviation from the regression line. The iterative method is based on discarding this line and on recalculation of the regression function. This procedure is repeated until the coefficient of determination exceeds a threshold value. By this algebraic approach, it is ensured that data points which appear as obvious outliers in every time window are discarded. As break condition for the iterative Boltzmann plot method, an average threshold value of $r^2 = 0.98$ is taken.

This iterative method stopped after discarding 106 Fe I lines and 36 Fe II lines. By this approach, relative errors for the electron temperature of 1.8% with the remaining 61 Fe I and 4.4% with 12 Fe II emission lines averaged over all considered nine time windows and laser pulse energies were achieved. These remaining emission lines for the temperature determination are summarized in Tables A.4 and A.5.

The development of the average relative error of the electron temperature for Fe I emission lines by iteration number is shown in Fig. A.3. As can be seen the averaged relative errors are decreasing by nearly a factor of three in the case of Fe I emission lines during the iterative process. Due to a couple of outlier emission lines in the case of Fe II emission lines which are considered in the beginning of the iteration process, the averaged relative errors are reduced by even a factor of 14.

Table A.4 Spectroscopic data of selected Fe I emission lines

No.	λ (nm)	A_{nm} (1/s)	E_n(eV)	g_n
1	244.256	2.14E + 08	7.508	11
2	282.328	1.86E + 07	5.349	7
3	289.942	5.92E + 07	6.554	3
4	295.999	4.81E + 07	6.880	13
5	299.039	3.90E + 07	6.873	11
6	301.148	4.70E + 07	6.875	9
7	301.898	1.26E + 07	5.064	7
8	302.403	4.87E + 06	4.209	5
9	303.015	4.79E + 07	6.524	11
10	305.307	1.53E + 07	6.484	5
11	305.526	8.63E + 06	5.615	5
12	307.572	2.94E + 07	4.988	5
13	308.374	3.01E + 07	5.010	3
14	309.158	5.41E + 07	5.021	1
15	328.026	5.38E + 07	7.080	11
16	331.474	6.89E + 07	7.041	7
17	336.955	2.42E + 07	6.406	9
18	337.078	3.29E + 07	6.370	11
19	338.011	2.35E + 07	6.426	7
20	341.313	3.57E + 07	5.830	7
21	342.266	2.79E + 07	5.845	5
22	342.712	5.49E + 07	5.793	9
23	347.545	7.01E + 06	3.654	5
24	349.057	4.47E + 06	3.603	7
25	349.529	9.46E + 06	6.106	7
26	351.382	3.40E + 06	4.387	11
27	360.668	8.24E + 07	6.129	13
28	364.951	4.22E + 07	6.089	9
29	365.147	6.23E + 07	6.153	9
30	367.763	8.01E + 07	6.129	5
31	368.411	3.36E + 07	6.092	7
32	369.073	2.74E + 07	6.932	11
33	370.557	3.21E + 06	3.397	7
34	372.256	4.97E + 06	3.417	5
35	372.438	1.25E + 07	5.607	7
36	376.554	9.69E + 07	6.529	15
37	376.719	6.39E + 07	4.302	3
38	379.955	7.31E + 06	4.221	9
39	380.535	9.81E + 07	6.559	11
40	382.782	1.05E + 08	4.796	5
41	384.326	4.67E + 07	6.272	7
42	384.997	6.05E + 07	4.231	1
43	385.637	4.64E + 06	3.266	5
44	386.552	1.55E + 07	4.218	3
45	386.722	3.39E + 07	6.223	5
46	387.376	8.01E + 06	5.633	9
47	392.026	2.60E + 06	3.283	3

(continued)

Table A.4 (continued)

No.	λ (nm)	A_{nm} (1/s)	E_n(eV)	g_n
48	392.291	1.08E + 06	3.211	9
49	395.116	3.56E + 07	6.411	5
50	397.774	7.01E + 06	5.314	5
51	401.453	2.37E + 07	6.661	11
52	404.581	8.62E + 07	4.549	9
53	406.359	6.78E + 07	4.608	7
54	407.174	7.65E + 07	4.652	5
55	410.749	2.45E + 07	5.850	3
56	421.936	3.80E + 07	6.511	13
57	430.790	3.40E + 07	4.435	9
58	432.576	4.97E + 07	4.474	7
59	436.977	7.22E + 06	5.884	9
60	438.354	5.00E + 07	4.313	11
61	440.475	2.75E + 07	4.372	9

Table A.5 Spectroscopic data of selected Fe II emission lines

No.	λ (nm)	A_{nm} (1/s)	E_n (eV)	g_n
1	224.550	2.61E + 08	10.289	10
2	233.131	2.92E + 07	5.549	8
3	234.534	8.46E + 07	7.920	12
4	236.860	5.93E + 07	5.585	4
5	237.519	9.81E + 07	5.605	2
6	238.076	3.14E + 07	5.289	8
7	257.792	1.26E + 08	5.905	2
8	259.154	5.11E + 07	5.824	6
9	261.383	1.99E + 08	4.849	2
10	262.829	8.56E + 07	4.837	4
11	263.957	1.07E + 08	8.036	2
12	271.441	5.48E + 07	5.553	6

Figure A.4 shows the development of the averaged coefficient of determination for Fe II emission lines.

The coefficient of determination in iteration step 37 exceeds the threshold value of $r^2 = 0.98$ so that in total 36 Fe II emission lines are discarded in this case. The corresponding Boltzmann plots are shown in Figs. A.5 and A.6. The relative temperature errors are reduced in this particular case to $\Delta T_e/T_e = 1.7\%$ for Fe I and $\Delta T_e/T_e = 5.9\%$ for Fe II emission lines. This effect is due to the fact that on average a certain coefficient of determination is required which in turn is responsible for the exclusion of emission lines with comparatively high residue to the regression line. The higher relative error for Fe II emission lines can be related to the lower number of remaining spectral lines compared with those for Fe I. This result is a consequence of the fact that ionized species in the plasma relax continuously to lower ionization stages.

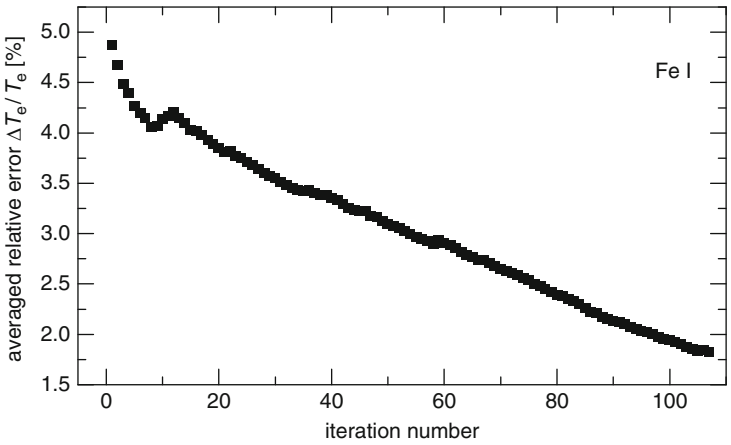

Fig. A.3 Development of the averaged relative errors of electron temperature derived with Fe I emission lines

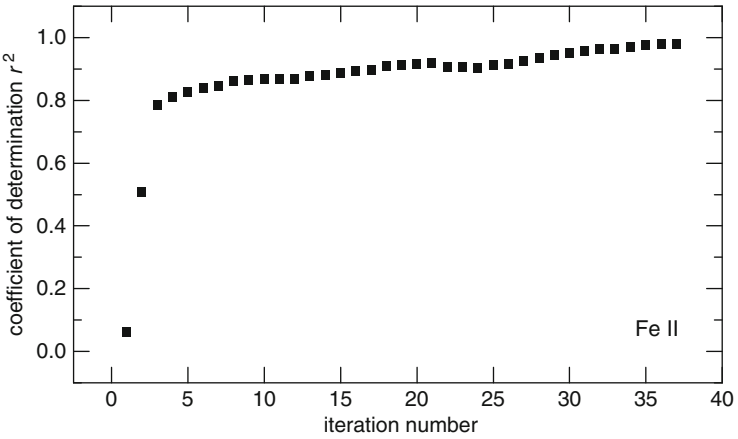

Fig. A.4 Development of the averaged coefficient of determination for the considered 36 Boltzmann plots vs. the iteration number for Fe II emission lines

In Figs. A.7 and A.8, the calculated electron temperatures are shown for the investigated pulse energies and delay times t_{delay}. For Fe I and Fe II, two different electron temperatures exist within the plasma. Starting from $t_{delay} = 100$ ns to $t_{delay} = 900$ ns for both ionization stages and most pulse energies the temperatures are decreasing. Comparing those values with the estimated electron temperatures at the beginning of the theoretical line preselection, the average electron temperature $T_e \sim 8{,}300$ K of the atomic lines for all investigated times and pulse energies is ~600 K below the chosen temperature at the beginning of the line selection process. In the case of the ionic lines, the average temperature $T_e \sim 12{,}200$ K is about 900 K

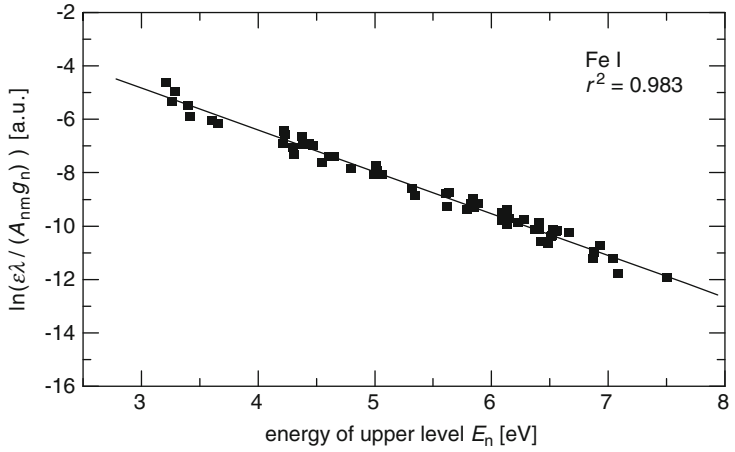

Fig. A.5 Boltzmann plot with 61 Fe I emission lines for an exemplarily chosen time window $t_{delay} = 900$ ns, $t_{int} = 100$ ns, $E_b = 0.5$ mJ. The relative temperature errors are $\Delta T_e / T_e = 1.7\%$ for this time window

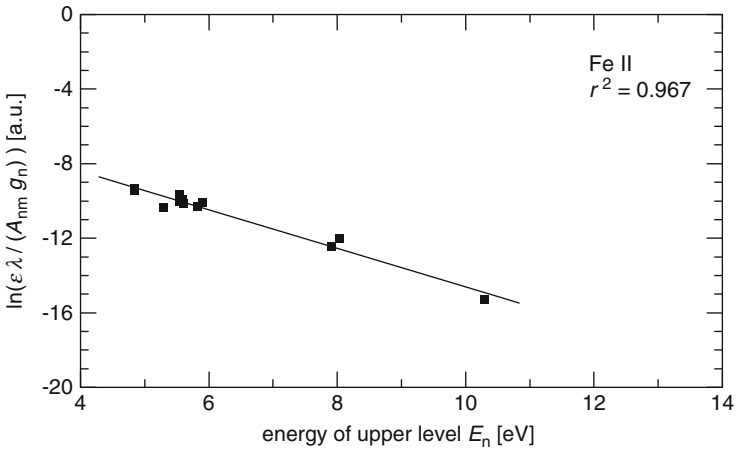

Fig. A.6 Boltzmann plot with 12 Fe II emission lines, other data as in Fig. A.5. The relative temperature error is $\Delta T_e / T_e = 5.9\%$

higher than the initial one. These average temperatures are in the same regime like those that were reported by Detalle et al. where electron temperatures between 7,000 and 10,000 K were detected using similar laser irradiances [A.31]. To determine the electron temperature, six Fe I spectral lines in the wavelength range between 370 and 380 nm were chosen. Only delay times between 100 and 400 ns were investigated, with an error of 37.5% for $t_{delay} = 400$ ns.

It should be noticed that the above-described iterative Boltzmann plot procedure is a systematic approach to improve the precision of the electron temperature

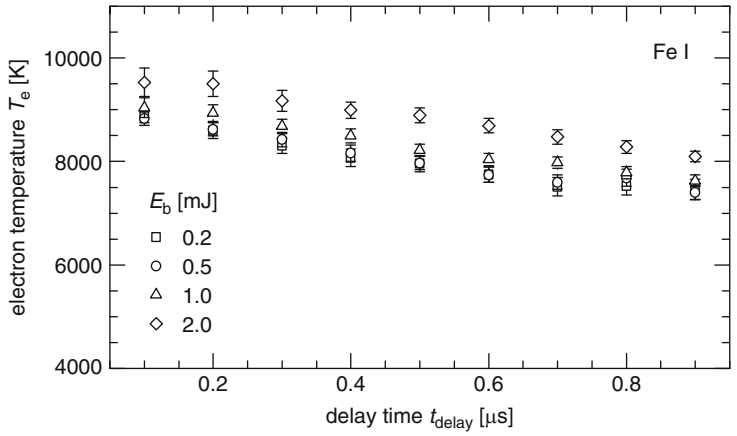

Fig. A.7 Electron temperatures determined by Boltzmann plots with 61 Fe I emission lines at different delay times for pulse energies between 0.2 and 2 mJ

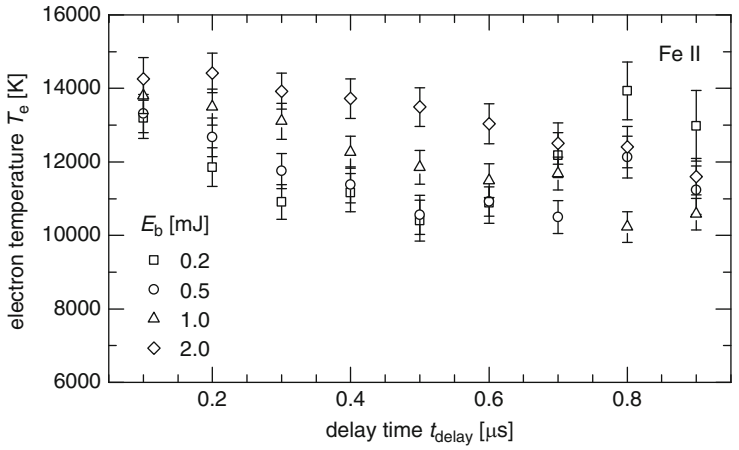

Fig. A.8 Electron temperatures determined by Boltzmann plots with 12 Fe II emission lines at different delay times for pulse energies between 0.2 and 2 mJ

determination. However, the reduction of the relative temperature errors does not necessarily imply an improvement regarding the accuracy. The assessment of accuracy would require a comparison between independent techniques for the determination of the electron temperature.

The results show that even at comparatively low laser pulse energies ($E_b \leq 2$ mJ) up to 61 atomic emission lines can be identified within a typical spectral range for temperature measurements. It should be mentioned that the chosen criteria within the proposed procedure were applied to achieve pragmatic but quantitatively well-grounded results for the experiment. In fact, this result improves the precision of

the electron temperature determination. The three main advantages of the described method are: the transferability to other problems, e.g., samples with arbitrary chemical composition; the quantitative validation between theoretical predictions and experimental data; the systematic approach to find appropriate spectral lines for LIBS applications.

References

A.1. N. Konjevic, M. Dimitrijevic, W. Wiese, Experimental Stark widths and shifts for spectral lines of neutral and ionized atoms, J. Phys. Chem. Ref. Data, **13**, 619–647 (1984)

A.2. C. Colon, G. Hatem, E. Verdugo, P. Ruiz, J. Campos, Measurement of the Stark broadening and shift parameters for several ultraviolet lines of singly ionized aluminum, J. Appl. Phys. **73**, 4752–4758 (1993)

A.3. N. Konjevic, W. Wiese, Experimental Stark widths and shifts for spectral lines of neutral and ionized atoms, J. Phys. Chem. Ref. Data, **19**, 1307–1385 (1990)

A.4. H. Griem, *Spectral Line Broadening by Plasmas*, (Academic, London, 1974), Appendix IV, p. 320

A.5. Z. Szymanski, J. Kurzyna, W. Kalita, The spectroscopy of the plasma plume induced during welding of stainless steel and titanium, J. Phys. D. Appl. Phys. **30**, 3153–3162 (1997)

A.6. J. Aguilera, C: Aragon, Curves of growth of spectral lines emitted by a laser-induced plasma: influence of the temporal evolution and spatial inhomogeneity of the plasma, Spectrochim. Acta B 58 221–237 (2003)

A.7. A. Lesage, J. Lebrun, J. Richou, Temperature dependence of Stark parameters for Fe I lines, Astrophys. J. **360**, 737–740 (1990)

A.8. M. Rösner-Kuhn, D. Matson, K. Drewes, U. Thiedemann, G. Kuppermann, M. Flemings, M. Frohberg, Enthalpies and heat capacities of liquid Fe-Cr-Ni alloys with the focus on pure liquid chromium, Thermochim. Acta **314**, 123–129 (1998)

A.9. A. Bartecka, T. Wujec, J. Halenka, J. Musielok, Experimental Stark-broadening studies of the N I multiplet at 7904.5 A, Eur. Phys. J. D **29**, 265–271 (2004)

A.10. S. Freudenstein, J. Cooper, Stark broadening of Fe I 5383 A, Astron. Astrophys. **71**, 283–288 (1979)

A.11. V. Bakshi, R. Kearney, Measurement of Stark width of some Ar I transitions in a d.c. argon plasma jet at atmospheric pressure, J. Quant. Spectrosc. Radiat. Transf. **42**, 405–413 (1989)

A.12. M. Dimitrijevic, S. Sahal-Brechot, Stark broadening of Ca II spectral lines, J. Quant. Spectrosc. Radiat. Transf. **49**, 157–164 (1993)

A.13. J. Puric, S. Djenize, A. Sreckovic, S. Bukvic, S. Pivalica, J. Labat, Stark widths of singly-ionized iron spectral lines, Astron. Astrophys. Suppl. Ser. **102**, 607–609 (1993)

A.14. M. Dimitrijevic, S. Sahal-Brechot, Stark broadening of Al I spectral lines, Physica Scripta **49**, 34–38 (1994)

A.15. K. Dzierzega, K. Musiol, Stark broadening and shift for Ar II lines, J. Quant. Spectrosc. Radiat. Transf. **52**, 747–754 (1994)

A.16. M. Dimitrijevic, S. Sahal-Brechot, Stark broadening of Mg I spectral lines, Physica Scripta **52**, 41–51 (1995)

A.17. E. Sarandaev, M. Salakhov, Regularities in the Stark widths and shifts of spectral lines of singly-ionized aluminium, J. Quant. Spectrosc. Radiat. Transf. **56**, 399–407 (1996)

A.18. J. Knauer, M. Kock, Experimental Stark broadening constants for Ar I, Ar and II Kr I resonance lines in the vacuum ultraviolet region, J. Quant. Spectrosc. Radiat. Transf. **56**, 563–572 (1996)

A.19. N. Nessib, Z. Lakhdar, Stark broadening of neutral oxygen lines in the impact and quasistatic approximations, Physica Scripta **54**, 608–613 (1996)

A.20. L. Popovic, M. Dimitrijevic, Stark broadening of heavy ion lines: As II, Br II, Sb II and I II, Physica Scripta **53**, 325–331 (1996)
A.21. NIST Atomic Spectra Database, Vers. 4, Lines, http://physics.nist.gov/PhysRefData/ASD/lines_form.html
A.22. V. Detalle, R. Héon, M. Sabsabi, L. St-Onge, An evaluation of a commercial echelle spectrometer with intensified charge-coupled device detector for materials analysis by laser-induced plasma spectroscopy, Spectrochim. Acta B **56**, 1011–1025 (2001)
A.23. M. Sabsabi, V. Detalle, M. A. Harith, W. Tawfik, H. Imam, Comparative study of two new commercial echelle spectrometers equipped with intensified CCD for analysis of laser-induced breakdown spectroscopy, Appl. Opt. **42**, 6094–6096 (2003)
A.24. Ü. Aydin, P. Roth, C. Gehlen, R. Noll, Spectral line selection for time-resolved investigations of LIBS plasmas by an iterative Boltzmann plot method, Spectrochim. Acta B **63**, 1060–1065 (2008)
A.25. P. Fichet, J.-L. Lacour, D. Menut, P. Mauchien, A. Rivoallan, C. Fabre, J. Dubessy, M.-C. Boiron, in *Micro LIBS Technique*, ed. by A.W. Miziolek, V. Palleschi, I. Schechter. Laser-Induced Breakdown Spectroscopy (LIBS) – Fundamentals and Applications (Cambridge University Press, Cambridge, 2006), ISBN-13: 9780511243042
A.26. C. Geertsen, J.-L. Lacour, P. Mauchien, L. Pierrard, Evaluation of laser ablation optical emission spectrometry for microanalysis in aluminium samples, Spectrochim. Acta B **51**, 1403–1416 (1996)
A.27. V. Detalle, J.-L. Lacour, P. Mauchien, A. Semerok, Investigation of laser plasma for solid element composition microanalysis, Appl. Surf. Sci. **138**, 299–301 (1999)
A.28. C. Hartmann, A. Gillner, Investigaion on Laser Micro Ablation of Steel Using ps-IR Pulse Bursts, *LIA Conference Proceedings 2007*, (LIA, Orlando, 2007), pp. 38–44
A.29. H. Bette, R. Noll, in *High-Speed, High-Resolution LIBS Using Diode-Pumped Solid State Lasers*, ed. by A. Miziolek, V. Palleschi, I. Schechter. Laser-Induced Breakdown Spectroscopy, Chap. 14 (Cambridge University Press, Cambridge, 2006), pp. 490–515
A.30. R. Kurucz, B. Bell, 1995 *Atomic Line Data, Kurucz CD-ROM No. 23* (Smithsonian Astrophysical Observatory, Cambridge, MA)
A.31. V. Detalle, J. Lacour, P. Mauchien, A. Semerok, Investigation of laser plasma for solid element composition microanalysis, Appl. Surf. Sci. **138–139**, 299–301 (1999)
A.32. S. Brym, R. Ciurylo, E. Lisicki, R. Trawinski, Pressure broadening and shift of the 326.1 nm Cd line perturbed by argon, Physica Scripta **53**, 541–544 (1996)
A.33. Z. Szymanski, J. Kurzyna, W. Kalita, The spectroscopy of the plasma plume induced during welding of stainless steel and titanium, J. Phys. D. Appl. Phys. **30**, 3153–3162 (1997)
A.34. S. Pellerin, K. Musiol, J. Chapelle, Measurement of atomic parameters of singly ionized argon lines – III. STARK broadening parameters, J. Quant. Spectrosc. Radiat. Transf. **57**, 377–393 (1997)
A.35. J. Val, J. Aparicio, S. Mar, Experimental Stark widths and shifts of several Ne I spectral lines, Astrophys. J. **513**, 535–541 (1999)
A.36. N. Konjevic, Plasma broadening and shifting of non-hydrogenic spectral lnines: present status and applications, Phys. Rep. **316**, 339–401 (1999)
A.37. N. Konjevic, A. Lesage, J. Fuhr, W. Wiese, Experimental Stark widths and shifts for spectral lines of neutral and ionized atoms, J. Phys. Chem. Ref. Data **31**, 819–927 (2002)
A.38. A. Bartecka, T. Wujec, J. Halenka, J. Musielok, Experimental Stark-broadening studies of the N I multiplet at 7904.5 A, Eur. Phys. J. D **29**, 265–271 (2004)
A.39. J. Hoffman, Z. Szymanski, Time-dependent spectroscopy of plasma plume under laser welding conditions, J. Phys. D. Appl. Phys. **37**, 1792–1799 (2004)
A.40. S. Bukvic, A. Sreckovic, S. Djenize, Mg II h and k lines Stark parameters, New Astron. **9**, 629–633 (2004)

Index

ABEL inversion, 154
Ablation
  burst number, 104, 105
  depth, 402
  efficiency, 105
  of mass, 97, 102
  rate, 36, 116
Absorptance, 75
Absorption
  coefficient, 26, 79, 124, 171, 180
  properties of air, 33
  surface, 75
  volume, 76
Abundance ratio, 355
Acousto-optic modulator, 120
Acrylonitrile butadiene styrene, 286
Additive correction, 260
Additive(s), 285
Adiabatic coefficient, 140
Aerodynamic diameter, 362, 373
Aerosol, 361
  analysis, size-dependent, 372
  generator, 373
  particle, 372
Air
  compressed, 154
  pressure, 111
  stream, 372
Airborne particles, 362
Alkali, 355
Aluminum, 264, 367, 461, 486
  cast alloy, 264, 449, 484
  depth profile, 416
  map, 477, 478
  nitride, 474, 475
  oxide, 475
  pure aluminum sample, 449
  resonance line, 201
  samples, 449
  scrap, 484
  secondary aluminum, 264
  shredded aluminum scrap, 264, 484
  wrought alloy, 264
Ammonium nitrate, 462
Analysis function, curve, 41, 42, 216
  chromium, 260
  copper, 256
  magnesium, 461
  nickel, 257, 461
  silicon, 258, 270, 316
Analyte
  line, 11
  signal, 291
Analytical
  resolution, 443
  resolving power, 289, 459, 460
Angle
  of detection, 67, 237, 253
  of observation, 39
Antimon, 293
Apparative broadening, 177, 178
Argon
  co-flow, 377
  flushed sample stand, 316
  laser, 120
Arsenic, 324
Artificial neural network, 278
ATLAS system, 429
Atomic abundance, 352
Attenuation, 193
Autofocusing unit, 300
Availability, technical, 469
Averaging
  spatial, 13, 36, 315, 472

R. Noll, *Laser-Induced Breakdown Spectroscopy*, DOI 10.1007/978-3-642-20668-9,
© Springer-Verlag Berlin Heidelberg 2012

Back illuminated CCD, 63
Background equivalent concentration, 215, 227, 250
BALMER line, 149, 351
Beam
  guiding optics, 56
  GAUSSIAN, 27
  parameters, 19
  propagation ratio, 28
  quality, 27
  waist, 28, 113
Black body emission, 171
Blast furnace, 356
  slipping, 359
Boltzmann
  distribution, 135
  factor, 135
  formula, 172
  plot, 133, 144, 262, 531
  statistics, 160
Borate bead analysis, 316
Bound-free radiation, 195
Breakdown, 345
Bremsstrahlung, 149, 167
Brillouin scattering, 61
Bromine, 286, 293, 297
  line, 288
Building materials, 327
Bulk
  analysis, 18, 41, 275
  characterization, 275
Burden level, 359
Burst
  energy, 25, 403

Cadmium, 224, 227, 297, 323
Calcium, 347, 373, 376
  line intensity, 378
  particles, 378
Calibration
  -free LIBS, 207
  multivariate, 310
  univariate, 310
Calibration curve, 12, 212, 350
  bromine, 298
  cadmium, 297, 298
  calcium, 347, 368, 373
  carbon, 241, 250
  copper, 322, 450
  hydrogen/carbon ratio, 353
  lead, 369
  nickel, 251
  nitrogen/carbon ratio, 354
  oxygen/hydrogen ratio, 353
  phosphorus, 234, 250
  silicon, 91, 450
  sodium, 377
  sulfur, 234
  thallium, 326
  zinc, 322
Capillary electrophoresis, 14
Carbide, 476
Carbon, 279, 352, 357, 462
  -dioxide, 351
  line, 281
  mapping, 483
Cassegrain optics, 56
C2-band emission, 283
Cement
  hydrated, 327
  samples, 328
Certified reference material, 238
Channeltron signal, 331
Charged-coupled device, 55, 62
Charge detection limit, 66
Charge neutrality, 193
Chlorides of metals, 363
Chlorine, 280
  line, 327, 331
  ultraviolet line, 337
Chromatic aberration, 58
Chromium, 323
Circulating materials, 359
Classification, 278, 284, 486
  performance, 302
CN emission bands, 355
Coating thickness, 406
Coefficient of determination, 219, 243, 250, 310, 451, 462
Co-flow, 374
Coherent anti-Stokes Raman spectroscopy, 1
Collision, inelastic, 492
Combustion engine, 350
Congruence, 239
Continuum
  emission of the plasma, 10, 324, 394
  intensity, 146
  peak, 31, 341
  radiation, 149
Conveyor belt, 266, 270, 484
Copper, 323, 370
  copper in aluminum, 453
  map, 483
Correlation coefficient, 90
Covariance, 291
  normalized, 292

Crater, 8, 34
contour plot, 405
cross section, 99
depth, 239, 392, 405
diameter, 107, 239, 366, 392
dimensions, 98
formation, 97
geometry, 431
volume, 98
Critical value, 214
Crosstalk, 431
Curves-of-growths, 189, 376
Cyanide emission, 462
Czerny-Turner spectrometer, 51

Damage threshold, 59
De Broglie wavelength, 162, 193
Debris, 393
Debye
number, 163
sphere, 162
Decarburization zone, 474, 483
Decision limit, 488
Decomposition temperature, 78
Delay time, 9, 66
Dendrite, 483
Depth
information, 404, 420
profile, 402, 416, 453
resolving power, resolution, 408, 453
Detector types, 62
Diamond polishing, 475
Dichroic mirror, 56, 266, 402
Differential mobility analyzer, 373
Diffusion dryer, 373
DIN 32 645, 333
Diode-pumped solid state laser, 19
Direct light channel, 253, 327
Direction of
incidence of the laser beam, 38
observation of the plasma emission, 38
Displacement
energy, 491
of ambient atmosphere, 491
Dissociation, 7
Doppler broadening, 173
Double pulse, 23, 24, 84
collinear, 84, 103
mode, 457
symmetric, 131
unsymmetric, 131
Down cycling, 488
Drilling depth, 102

Droplet, 339, 373
generator, 339
picoliter, 340
Duplex, 438
Dust separator, 357
Dye laser, 223
Dynamic range, 65

Echelle spectrometer, 53, 287, 290, 351, 366, 375, 403
Einstein
coefficient of spontaneous emission, 133, 170, 195
coefficient of stimulated emission, 195
transition probability for absorption, 172
Ejection, 484
Electron
density, 133, 140, 146, 147, 157, 261, 332
density, spatially resolved, 152, 158
free, 154
ion collision frequency, 80
probe microscopy, 483
temperature, 132, 140, 146, 147, 262
Element
in alphabetic order allocated to wavelengths, 523
list of wavelengths, 511
maps, mapping, 393, 396, 476
-specific wavelength, 10
Emission
coefficient, 193
coefficient of free-free transistions, 167
coefficient of recombination radiation, 167
line, 31
spectrum of laser-induced plasma, 9
Energy buffer, 148
Enthalpy of the plasma, 203
Equilibration time, 164
Equivalence ratio, 350
Error, type 1, type 2, 486
Evaporation, 7, 75
temperature, 76
Expansion
adiabatic, 140
of planar shock front, 126
spherical, 126, 491
velocity, 125
Explosion, 125
Explosive residues, 462
Extinction coefficient, 193

Feedforward network, 284
Ferrite, 483

Fiber
optics, 57, 301, 467
UV-enhanced, 350
Flame retardants, 285
brominated, 285, 298
Flow rate, 103, 253
Fluence, 366
FML instrument, 448
Focal position, 141
Focusing
dynamic, 300
static, 300
Foil thickness, 116
Fraction pureness, 284
Framing images, 122, 153
Free-bound radiation, 196
Free-free radiation, 196
Free parameters, 197
Frequency distribution of emission signals, 481
Fringe displacement, 127, 154, 155
Front illuminated CCD, 63
F-value, 52

Gallilean telescope, 56, 455
Galvanized coatings, 401
Galvanizing plant, 424
Gas
accumulated, 492
ambient, 102, 367
ambient atmosphere, 29, 491
carrier, 372
density, 107, 191
exchange, 21, 67, 394
exchange time, 67
inert, 102
influence of gas pressure, 330
local gas exchange time, 21
mixtures, 105, 349
nozzle, 408
pressure, 374
reduced ambient pressure, 110
Gauss
distribution, 480
function, 173
width, 177
Glan
laser prism, 433
THOMPSON polarizer, 119
Grating, 52

Hand-held measuring pistol, 449
Heat
affected zone, 34
conduction, 114
penetration depth, 26, 34
stabilizer, 286
Heavy metal, 286
concentration in polymer matrix, 297
in soil, 319
Helium pressure, 330
Heptane, 350, 355
Heuristic modeling, 187, 190, 197
High-pressure liquid chromatography, 14
High-speed
camera, 344
framing images, 119
identification of scrap pieces, 484
LIBS, 388
photography, 120
scanning LIBS, 473
streak images, 119, 492
Hot-dip
coated sheet metal, 454
galvanized samples, 419
Hydrogen, 279, 357, 462
BALMER series, 280
line, 283
signal, 359
Hyphenated
HPLC-LIBS, 339
LIBS-LIF technique, 323
technique, 221, 337

Identification
correctness, 485, 488
of material mix-ups, 438
method, 275
of scrap pieces, 41
yield, 485
Impactor
cascade, 362
low-pressure, 362
Inclusion
analysis, 398, 475
concentration, 480
non-metallic, 481
size, 481
in steel, 397
types, 476
In-cylinder diagnostics, 350
Index of refraction, 152
Inductively coupled plasma atomic emission spectroscopy, 83
Industrial applications, 429, 467
Inline analysis, 2
analysis of galvanized sheet steel, 415

analysis of magnesium zinc coatings, 426
LIBS analyzer, 299
monitoring of the depth profile of Al in hot-dip galvanized coatings, 416, 426
process control, 437
In-situ analysis of heavy metals in soils, 320
Inspection
equipment monitoring, 469
machine, 440
Integration
time, 65
window, 9, 10
Interaction volume, 21
Interelement correction, 218, 260
Interference fringes, 154
Interferometric measurement, 121
Internal standardization, 211, 259, 291
Interpulse separation, 24, 108, 143
Ionization
degree, 146, 149
stage, 514
Iron, 357, 361
emission line, 133, 527
liquid pig iron, 462
matrix, 461
neutral iron atoms, 159
pure iron sample, 249, 445, 476
singly ionized iron ions, 159
spectrum, 198
Irradiance, 2, 8
of incident laser beam, 185
threshold, 43
ISO 9001, 469

Kirchhoff's law, 172, 195

Laboratory systems, 429
Lance, 248
Landau length, 161
Laser
absorption spectroscopy, 3
-induced breakdown spectroscopy, 2, 8, 12
-induced damage, 58
-induced fluorescence, 3, 14, 320
-induced fluorescence signal, 324
line section sensor, 484
measuring methods, 1
power, 469
radiant exposure, 107
sorting system, 484
spectroscopic methods, 1
triangulation sensor, 300
types, 47
Lead, 289, 324, 355, 357, 370
LIBS instruments, 429
Life time of the plasma, 8, 160
Light elements, 246
Light metal
alloy, 265
cycles, 488
Limit of detection, 214, 235, 241, 250, 267, 288, 294, 299, 323, 334, 347, 369, 436, 451, 462
Limit of identification, 215
Limit of quantification, 215
Line
broadening, 173
broadening, natural, 169
broadening, pressure, 169
emission coefficient, 168, 208
pairs, homologous, 211
radiation, 167
-ratio, 208
selection, 408, 511
shape, 348
shape function, profile, 169, 195
Line-to-background emission, 90
Line-to-continuum intensity, 145
Linear
calibration function, 250
dispersion, 51
Loading, 307
Local
dilution, 107
temperature equilibrium, 144, 162, 193
transient reduction of particle density, 159
Lollipop samples, 462, 482
Long term stability, 312
Lorentz
curve, 133
function, 169, 173, 201
Luminous front, 124

Mach number, 126
Mach-Zehnder interferometer, 120
Magnesium, 349
Magnesium fluoride
lens, 328
window, 329
Mandel test, 212
Manganese, 437, 462
map, 397, 476
Mass throughput, 488

Material
ablation, 21
identification, 442
organic, 462
recycling, 275, 488
vapor, 491
Matrix
effect, 262, 311, 368
element, 11
Maxwellian velocity distribution, 160
Mean, 481
Measuring
bursts, 306
frequency, 17, 66
method, 207
parameters, 14
position, 434
probe, 356, 358
procedure, 14
pulses, 14, 39, 212, 253, 437
volume, 467
Measuring chamber, 12, 66, 222, 223, 374, 389
pressure inside the measuring chamber, 327
volume, 67
Median, 481
Melt
analysis, 249
composition, 245
phase, 97, 245
Mercury, 289, 324
lamp, 456
Metal-salt solutions, 320
Microanalysis, 387, 472
scanning, 41, 390
Microchannel plate, 55, 62
Microlens array, 38, 315, 472
Mix-up
detection of material mix-ups, 467
Mobile systems, 447
Molar
concentration ratio, 370, 371
mixing ratio, 364
Molybdenum, 444
Moving
particles, 265
samples, 270
Multi-CCD Paschen-Runge system, 455
Multi-channel integrator electronics, 65, 231, 237, 288, 329, 356, 390, 417, 433, 435
Multi-element analysis, 2
Multiple laser pulses, 84
Multiplets, 199
Multiplicative correction, 260
Multivariate analysis, 318, 408, 471

Natural line width, 175
Nd:YAG laser, 47
continously-pumped, 19
diode-pumped, 48, 51
flashlamp-pumped, 17
Near infra-red, 276
Nickel, 324
high nickel alloys, 438
Nitride, 476
Nitrogen, 352, 357
flow, 361
map, 478
Non-conducting materials, 275
Non-metal elements, 340
Nozzle, 394
Nucleating agents, 286
Numerical aperture, 52
NEWTON
method, 193
telescope, 58, 455

Optical penetration depth, 26, 76
Optical probe, 247
Optical thickness, 172, 410
optically thick, 196
optically thin, 197
Ore, 359
Oscillator strength, 170, 181
Outlier points, 481
Oxide, 476
Oxygen, 352, 357
map, 477, 478

Partial least square algorithm, 307, 409
Particle
diameter, 370
number, 363
size distribution, 373
Particulates, 361
Partition function, 169, 193
Partition of laser burst energy, 131
Paschen-Runge spectrometer, 53, 265, 301, 342, 356, 372, 379, 388, 389, 417, 433, 437, 448, 455, 469, 472
Pearlite, 483
Pellets for XRF analysis, 315
Penetration depth per laser pulse, 453
Phosphor
map, 483

Photocathode sensitivity, 63
Photodiode
  array, 55
  signal, 343
Photomultiplier
  signal, 30, 88, 309, 394
  tube, 53, 62, 231
Physical model, 185
Piezoelectric nozzle, 339
Pigments, 285
Pipe fittings, 438, 467
Planck's law, 171
Plasma
  air-breakdown, 87
  characteristic time of decay, 190
  confinement, 131, 378
  core, 190
  dynamics, 119, 123, 131
  expansion, 124, 345
  geometry, 121, 431
  ignition, 366
  light-emitting, 87
  luminous front, 345
  parameter, 260
  residuals, 394
  shell, 190
  volume, 139
Plastic bottles, 277
Pneumatic dispatch, 430
Pockels cell, 23, 111
Polarizability, 154
Polarization coupling, 350
Polyamide, 27
Polycarbonate, 27
Polymer samples, 278
Polyvinyl chloride, 275
Portable systems, 447
Positive-intrinsic-negative-photodiode, 276
Potassium, 357
Pre-bursts, 306
Precision, 216
Preconditioning effect, 337
Prediction error, 471
Pre-pulses, 14, 40, 212, 442, 451
Principal component analysis, 479
Profiling of the spectrometer, 444
Propane, 350
  gas mixtures, 353
Publications on laser-induced breakdown spectroscopy, 4
Pulse, 22
  built-up time, 391
  energy ratio, 104, 402, 457
  femtosecond, 22
  nanosecond, 22
  picosecond, 35
  width, 104
Pulse-to-pulse fluctuations, 20
Pulse width, 22

Q-switching
  electro-optical, 17
Quantitative analysis, 207
Quantum efficiency, 63
Quartz fiber bundle, 276
Quasi-static broadening by ions, 173

Radiance of emission line, 179
Radiation processes, 167
Radiation transport equation, 193
Rarefied ambient atmosphere, 131
Ratio of ablation rates, 116
Rayleigh
  criterion, 52
  length, 28, 113
Recalibration, 216, 443, 469
Recombination
  energy, 140
  radiation, 167
Recycling of aluminum scrap, 484
Redeposition, 107
Reference line, 211
Reference samples, 11, 254
  certified, 11
  certified binary reference ZnAl-bulk sample, 420
Reflectivity, 77
Refractive index, 154
  distribution, 154
Refractor plate, 348
Regions of interest, 280
Regression
  analysis, 212
  least square, 471
  multilinear regression, 270
Relaxation time, 164, 165
Remote LIBS system, 454
Repeatability, 313
Repetition
  rate, 17
  time of laser pulses, 161
Residual, 216
  deviation, 256, 257
Resolution
  depth, 33, 36
  lateral spatial, 34, 387

spatial, 33
spectral, 88
thickness, 402
Resolving power of a spectrometer, 51
Resonance line, 188
Response time, 430
Root mean square error, 409
of prediction, 471
Rowland circle, 53

Scanner, 432, 468, 484
Scanning, 265
LIBS, 388
mobility particle sizer, 373
Score plot, 480
Scrap particles, pieces, 264, 485
Second harmonic generation, 222
Segregation
analysis, 398, 474, 482
ratio, 482
Self-absorption, 92, 180, 188, 377, 410
Self reversal, 201
Sensitivity, 213
Separation techniques, 349
Shell model of the plasma, 189
Shock wave, 125, 151
concentric, 156
propagation in inhomogeneous atmosphere, 130
Signal-to-noise ratio, 288, 289, 295, 341
Silicon, 462, 486
line, 308
Simulated plasma emission spectra, 32
Simulated spectral radiant flux, 197
Single pulses, 25, 83
Sinter, 358
Size-dependent
composition, 361
particle mass concentration, 379
Skewness, 480
coefficient, 482
Slag, 303
analysis, 303, 469
components, 315
converter, 304
lime saturated, 315
liquid slag, 462
vacuum, 317, 471
SML system, 473
Sodium, 344, 357, 360, 373, 376
Soil, 224
contaminated soil sample, 226
Solid sample, 14
Solid state laser
diode-pumped, 47, 388
flashlamp-pumped, 47
Sort identification, 451
Sorting plant, 302
Sound velocity, 21
Source apportionment, 361
Space exploration, 454
Spark optical emission spectrometry, 33, 229
Spatially resolved LIBS analysis, 43
Speciation analysis, 337
Spectral background, 295
Stability of the spectrometer, 473
Standard deviation
of procedure, 266
relative standard deviation of procedure, 213, 268
residual standard deviation, 213
Stark
broadening, 133, 149, 159, 173, 198, 260, 281
broadening parameter, 173
coefficient, 134
data, 511
quadratic STARK effect, 173, 194
red shift, 201
shift parameter, 174, 199
width, 149
State of aggregation, 42
Steel, 229
electrolytic galvanized sheet, 404
high alloyed steel foils, 112
high-alloy steel, 252, 254, 467
liquid, 245, 249, 251
low-alloy steel, 232
moving sheet, 401, 403
rotating sheet steel disks, 418
stainless, 438
thin sheets, 475
with scale layer, 235, 433
Stoichiometric ratio, 279
Streak
camera, 120
photographs, 123
Sulfide, 476
Sulfur, 314
map, 397, 482
Superduplex, 438
Swan bands, 280

Table-type circular conveyor, 440
Tailored pulse train, 94
Target function, 309

TeleLis system, 455
Temperature correction, 409, 412
Temporal width of laser pulse, 160
Thallium, 225, 324
Thermal conductivity, 108
Thermal diffusivity, 26, 34, 114
Thickness
  of coatings, 401
  resolution, 415
  of scale layers, 429
Time scales, 160
  electron-electron relaxation time, 161
  electron-ion relaxation time, 161
  electron-neutral relaxation time, 161
  gas exchange time, 21, 67
  population of levels, 161
Titanium, 438, 486
  nitride, 475
Top gas, 356
  tube, 358
Transmittance
  of CaF_2, MgF_2 windows, 58
  of silica fiber optics, 58
Triangulation sensor, 418, 440, 446
Triple pulses, 24, 236, 416
  collinear, 92
Trueness, 313
Tube, 467
Tunable laser source, 223
Two-step technique, 83

UNSÖLD's formula, 146, 169

Vacuum
  degasser, 315, 472
  spectrometer, 389
  ultraviolet, 32, 67, 287
Vapor density, 78
Velocity of measuring object, 41
Vibrating chute, 484
Voigt profile, 174, 409

Warming-up pulses, 39, 212
Waste electric and electronic equipment, 285
Water droplets, 341
Weld seam, cross section, 398
Wet-chemical methods, 475
White light interferometry, 405
Wires of steel belt tyres, 475

X-ray fluorescence, 229
  analysis, 304

Zeroth order, 469
  of the grating, 306
Zinc, 324, 355, 357, 360, 371
  coating, 403